Detecting oil in sea ice using Ground-penetrating radar: Developing a new airborne system

January 2012

Detecting oil in sea ice using Ground-penetrating radar: Developing a new airborne system

January 10, 2012

Prepared for:

Bureau of Safety and Environmental Enforcement (BSEE)

Contract # E12PC00010

Submitted by:

DF Dickins Associates, LLC

David Dickins
dfdickins@sbcglobal.net

Boise State University (CGISS)

John Bradford
johnb@cgiss.boisestate.edu

Hans Peter Marshall
hpmarshall@boisestate.edu

Robert Hay
roberthay@boisestate.edu

ACKNOWLEDGEMENTS

The authors wish to express their appreciation for the excellent support provided by the staff at CRREL led by Len Zabilanski. Their efforts made the test program possible, by growing the test ice sheet, assisting the field measurements, and documenting the ice properties essential to interpreting and correctly modeling the radar results.

PARTICIPANTS

This project was funded by the following participants:

- Alaska Clean Seas
- ConocoPhillips
- ExxonMobil Upstream Research Company
- Shell International Exploration and Production
- Statoil Petroleum
- United States Government, Bureau of Safety and Environmental Enforcement

Summary

Initiated in 2009, the current oil-in-ice Ground Penetrating Radar (GPR) project differs from the previous work in this field by focusing on new hardware development to design and fabricate prototype, higher-powered and more directional radar systems that can be tested in Arctic field environments using commonly available light helicopters. The goal is to significantly expand the practical operating window for oil detection with GPR to cover a wider range of sea ice and climate conditions extending to thicker and warmer (more conductive) ice sheets in late winter.

The overall purpose of the latest project running through 2010 and 2011 is to develop an airborne (low altitude) radar system with the goal of determining the presence of a relatively thin layer of oil under saline ice. To meet this challenge the radar development team from Boise State University (BSU) custom designed and fabricated a new GPR system that incorporated significant technological improvements over currently available commercial products.

The new system operates in a frequency range optimized for measuring oil under sea ice with antennae designed to greatly increase the directionality of the transmitted signal. Due to the RF absorption of saline ice, it was determined that the upper frequency needed to be limited to 2 GHz. A lower frequency limit of 500 MHz was dictated by the bandwidth of the horn antennas. A Frequency Modulated Continuous Wave (FMCW) architecture was selected to provide several clear benefits over the pulse radars previously tested, including:

- Avoids the need to develop high-energy impulses associated with pulse radar,
- Uses the maximum available spectrum to achieve the optimum distance resolution.

The hardware for the original prototype radar was completed in late 2010, capable of using either horn-based antennas, or a larger horn-fed reflector dish.

The test program incorporated two components:

1. Trials with crude oil spilled underneath an artificially grown 92 cm thick ice sheet in large outdoor basin at the US Army Cold Regions Environmental Laboratory (CRREL). The radar was supported above the ice on a moving overhead gantry frame.
2. Trials without oil over natural sea ice anticipated being in the range 1.7 to 2 m thick off Prudhoe Bay. The radar in this case would be mounted under the belly of a Bell 206L using the FAA-approved bracket purchased through the project.

The findings from the CRREL test program described in detail in this report, did not support proceeding with the planned 2011 airborne field tests in Alaska and pointed to the need for a number of design modifications primarily aimed at improving the Signal to Noise Ratio (SNR). These are summarized in Chapter 6 and detailed in Attachment 1.

Key findings from the 2011 radar test program are summarized in the following points:

- In the 2011 basin tests, the commercially available GPR (used in previous tests dating back to 2004) clearly differentiated oiled areas from clean when operated both from the

ice surface and (with substantial post-processing) when suspended above the ice at a height of ~3 m under temperature conditions representative of late winter in the Arctic.

- The 2011 CRREL tests with the commercial radar confirmed previous findings with an average detectable film thickness of 3.6 cm (range from ~1.4 to 4.4 cm).

- Very weak currents in the underlying water body can produce strong anisotropy in the sea ice crystal structure and resulting electrical properties. Containment skirts inserted during ice growth appear to sufficiently alter water circulation patterns that significant differences in ice anisotropy are observed across skirt boundaries. This effect was observed in the 2006 field test in Svea, Norway and again during this test in the outdoor basin at CRREL. Similar effects are also experienced in natural sea ice and need to be accounted for in future radar design and operation.

- As expected, high noise levels were observed when the commercial radar was mounted on a steel gantry. However, it was still possible to effectively extract the oil target reflection with in areas where the antenna polarization was optimally aligned with the ice anisotropy.

- Numerical modeling of the pulsed radar with electrical properties derived from ice temperature and salinity measurements are in close agreement with the field traces and correctly predict changes in amplitude, phase, and frequency content that are caused by oil within and beneath the ice.

- The Frequency Modulated Continuous Wave (FMCW) radar system, due to its much improved directionality compared to the commercial pulsed system, showed no decrease in (Signal to Noise Ratio) SNR between handheld measurements over the ice, and when mounted to the gantry. These results indicate that mounting on helicopter should not result in a significant increase in noise. This was one of the initial objectives in developing the new system based on FMCW architecture.

- The new FMCW radar system successfully profiled the surface of the ice, with a very stable signal. However, the new system was unable to reliably detect the bottom of the ice or the oil, due to an elevated signal-to-noise-ratio (SNR). Reducing the SNR to the necessary target level became a primary goal of a series of design modifications implemented following the 2011 CRREL test program (summarized in Chapter 6 and detailed in Attachment 1).

- A fully redesigned and improved FMCW system incorporating the recommended modifications was completed in December 2011 in anticipation of further testing at CRREL proposed for late January 2012. Based on the outcome of this second series of tests, a decision will be made early in 2012 whether to reinstate the airborne tests over thick sea ice at Prudhoe Bay originally planned for the spring of 2011.

Table of contents page

1. Background 1
1.1 State of Knowledge 1
1.2 Evolution of the Radar Design Program 1
1.3 Evolution of the Radar Test Program 2

2. 2011 CRREL Test Program: Introduction 3

3. Test Layout and Preparation 4

4. Ice Sheet Growth and Properties 8
4.1 Thickness and Temperature 8
4.2 Ice Coring and Drilling Results 11

5. Radar Data Interpretation 16
5.1 Commercial Radar Tests 17
5.1.1 Ground coupled profiling 19
5.1.2 Off-ice profiling 23
5.1.3 Expanding spread gathers 26
5.1.4 Modeling 27
5.2 FMCW radar results 29
5.2.1 Experiments on the ice surface 32
5.2.2 Experiments on the gantry 33
5.2.3 Signal to Noise ratio analysis 34
5.2.4 FMCW radar profiles from gantry 35

6. 2011 Radar Design Improvements 37
6.1 Introduction 38
6.2 Design Objectives 38
6.3 Design Architecture and Construction 38

ATTACHMENT 1: Design and Construction of the improved FMCW System

1. Background

1.1 State of Knowledge

The current state of knowledge surrounding GPR capabilities for oil-in-ice detection is summarized briefly below as a baseline.

- Previous tank testing at CRREL (2004) and in field tests in Norway (2006) demonstrated that a surface-based ground-penetrating radar (GPR) operating at 500 MHz can clearly delineate changes at the ice water interface caused by emplacement of oil. Testing at CRREL in March 2011 showed that commercially available GPR operated from the ice surface and up to a height of ~3 m is capable of differentiating oiled from clean ice under freezing conditions with relatively cold ice sheets. Previous attempts to fly this unit at low altitude (5-10 m) in Norway in 2006 showed that it was incapable of profiling the ice undersurface or detecting oil with a relatively warm ice sheet.

- Earlier results indicating a realistic lower detection limit in the order of 1 to 2 cm oil film thickness were confirmed in the 2011 CRREL where the average oil film thickness was 1.4 cm (0 to 3.5 cm range).

- The existing, portable commercial GPR systems are capable of profiling natural sea ice sheets from the surface at least as thick as 2 m as late as April (warmer ice later in the ice season could reduce the allowable thickness). This claim is based on the results of the April 2005 trials with ACS at Prudhoe Bay.

1.2 Evolution of the Radar Design Program

Initiated in 2009, the current oil-in-ice GPR project differs from the previous studies by focusing on new hardware development to design and fabricate prototype, higher-powered and more directional radar systems that can be tested in Arctic field environments using commonly available light helicopters (Bell 206L, AS350 or equivalent). The goal is to significantly expand the practical operating window for oil detection with GPR to cover a wider range of sea ice and climate conditions extending to thicker and warmer ice sheets in late winter.

A critical long-term objective in developing and testing GPR applications for oil spills in ice has always been the development of a reliable airborne system that can tolerate a wide range of ice properties; for example internal temperatures at mid-depth in the -4 to -5°C range representative of late April conditions in the Beaufort Sea. The internal ice temperatures during the test week at CRREL in March 2011 fell within this range, providing a realistic simulation of Arctic late winter conditions.

To meet the challenge of extending the reliable operating window for GPR beyond mid-winter when sea ice conductivity is at a minimum, the project team custom designed and

fabricated two new GPR systems that incorporated significant technological improvements over currently available systems. The new systems operate in a frequency range optimized for measuring oil under sea ice with antennae designed to greatly increase the directionality of the transmitted signal. The combination of a more focused beam and the flexibility to choose the optimal frequency for a given ice condition greatly increases the potential signal-to-noise ratio (SNR) with the goal of enhancing the probability and accuracy of detecting oil under ice in a wider range of conditions.

The hardware for the two new systems was completed in late 2010, with one system using horn-based antennas, and a second system using a horn-fed reflector dish. As presently configured, with the FAA-approved belly mount purchased through the project, the horn antenna system will mount on any Bell 206L helicopter, in common use throughout North America, including Alaska. With different mounting brackets it should also be possible to fly the same system on a range of different helicopters in use worldwide, for example the Aerospatiale AS-350. The horn-fed reflector dish will require additional engineering beyond the scope of this project before airborne operation, but gives us a comparison of the advantages of increasing the directionality of the radar beam compared to the horn system.

Prior to the 2011 testing at CRREL (see below), work focused on development of the data acquisition, control, and processing software for the two new radar systems. Modifying the existing BSU radar technology from the microwave region (2-18 GHz) to the frequencies optimal for this project (0.5-2GHz), led to some unexpected challenges. A much larger source current was required to drive the analog signals, which control the new 0.5-2 GHz oscillator, requiring new data acquisition hardware, and development of new data acquisition and control software. An unresolved problem with high noise levels in the new oscillator across the primary frequency range of interest led to substitution with a high-quality lab oscillator during the actual test program. A new oscillator is incorporated in the redesigned radar to overcome these problems, along with other modifications detailed in Attachment 1.

1.3 Evolution of the Radar Test Program

The initial project proposal conceived in 2009 was based on testing locally over fresh-water ice in Idaho. Based on a realistic radar design and build schedule, it was decided early on to replace these tests with more realistic field trials at Prudhoe Bay over thicker sea ice at no additional cost to the project (with ACS logistics support in kind).

Subsequent discussions with the participants showed a strong preference for testing with real oil, something not possible in a natural field setting. After reviewing available options, it was determined that a large outdoor test basin at the CRREL facility in Hanover NH could be used to grow a substantial sea ice sheet while being able to spill oil under the ice in a controlled setting.

As detailed in results described in this test report, the commercially available pulse radar operating at 500 MHz was markedly superior to the new “airborne” radar prototype in

the March 2011 tests. In addition, the commercial system was able to detect an average oil thickness of 1.3 cm trapped in the lower few centimeters of an 84 cm (avg.) ice sheet while suspended at a 3 m height from the gantry.

Following the CRREL program in 2011, the decision was made to postpone the planned 2011 Prudhoe Bay test program to fly the new radar system and reallocate the remaining funds to allow major design improvements to be carried out through the remainder of the year (summarized here in Section 6 and in further detail in Attachment 1).

2. 2011 CRREL Test Program: Introduction

The two new frequency modulated systems together with the existing pulse radar were extensively tested through multiple runs on the ice surface, and while fastened to the moving steel gantry and suspended at different heights. A resistivity profile of the ice over the full tank length was conducted as well as measurements of the dielectric properties of ANS crude oil acquired from Ohmsett.

In addition to the ongoing automatic monitoring of the ice temperature at different depths, CRREL staff carried out a comprehensive series of ice measurements through the test week including cores through unoiled ice areas to document thickness and salinity variations in the tank, multiple drill holes in each oil test hoop to document the ice thickness variability and, in the case of the first spill, the thickness of ice that had grown beneath the oil as well as the depth of the trapped oil layer, and underwater video of both test hoops showing areas with and without oil.

The primary objectives of the 2011 CRREL tests were to:

1. Validate the radar performance predictions from modeling with a radar experiments on a controlled ice sheet of known temperature, salinity and thickness and oil spills of known volume, and average thickness.

2. Provide a comparison of the parabolic and horn antennae to guide future oil-in-ice GPR development priorities.

3. Provide a comparison the performance of the new radar systems with a commercially available off-the-shelf system used in previous tests at CRREL (2004), Prudhoe (2005) and Svalbard (2006, 2008).

The 2011 test layout, ice characteristics and radar results are summarized in the following sections 3 through 5.

3. Test Layout and Preparation

The project utilized the Geophysical Research Facility at CRREL to develop a test sea ice sheet. This facility consists of a concrete basin, 18.25 m long × 6.7 m wide × 2 m deep (60 × 22 × 7 ft), with a removable roof that grows and maintains a growing ice cover in a refrigerated ambient environment and protects it from snow and rain (**Fig. 1**).

Figure 1. Geophysical Research Facility test basin before being filled with salt water.

Most important for testing the radar systems in an "airborne" mode, was the fact that the tank incorporates a moving gantry that runs the full length of the basin on rails (**Fig. 2**). This provided a convenient mounting point for the two new antennae.

To assist with determining the oil spatial distribution under the ice (not thickness) CRREL developed a towed underwater camera system than could be moved along the tank on a track laid along the tank centerline. The wide-angle camera was tilted to either side of vertical to cover the full width of each test area. (**Fig. 3**).

Figure 2. Test facility showing the two hoops frozen in and the moving gantry.

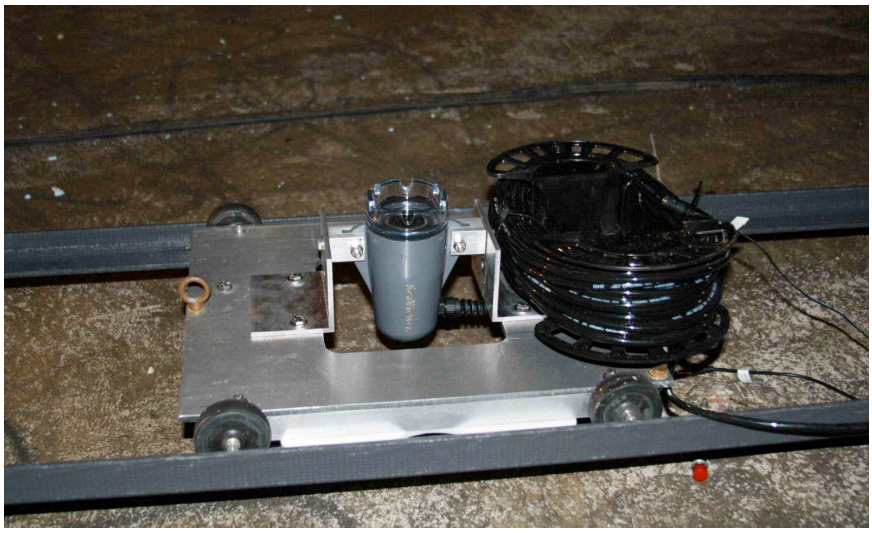

Figure 3. Underwater camera looking vertically up under the ice – shown mounted on its dolly rolling on an underwater track running the full length of the basin.

Two square (16 $m^{2)}$ fabric skirts with a flotation collar were allowed to freeze in to contain the oil. The skirt depths from the top of the ice were 123 cm and 171 cm respectively for Hoops 1 and 2. The corresponding skirt depths beneath the ice at the time of the two spills were ~38 cm for Hoop 1 and 79 cm for Hoop 2.

Fig. 4 shows the two hoops anchored in place just before the roof was pulled into place. The upright between the containment hoops is a thermistor string with probes every 10 cm which was frozen into the ice sheet and monitored the ice temperature throughout the growth cycle and test period (**Fig. 7**). Water salinity in the tank at the onset of freezing was 15.8 ppt. The starting salinity was deliberately chosen to be less than standard seawater to compensate for the fact that as the ice grows, the majority of the salts are increasingly concentrated in an ever-smaller volume of water. In this manner, a realistic Arctic Ocean salinity below the ice of 32% was achieved at the end of the growth cycle. The water beneath the ice was recirculated to guard against an artificial spike in water salinity occurring within the semi-enclosed water mass inside the skirted areas.

Figure 4. View looking north showing the two test hoops (skirts) with their flotation collars anchored in position immediately prior to freezing a continuous ice sheet. Thermistor string with data cable installed vertically between the two oil test areas.

Two spills were conducted, the first on February 18 prior to testing to allow the oil to become encapsulated by new ice growth, and the second on March 2 during the actual GPR surveys. In each case the discharge hose was positioned in the center of the skirt with the same trolley system used for the underwater camera (**Fig. 3**). **Figs. 5 and 6** below show the oil tote used to transfer and store the ANS crude donated to the project by the BOEMRE (now BSEE) Ohmsett facility in New Jersey and the oil being injected under Hoop #2 with a hose run through a plywood lined access hole at the North end of the basin.

Figure 5. Pumping oil from the tote into Hoop 2 through the camera access hole at the north end of the tank.

Figure 6. Oil tote used to transport and store oil shipped from Ohmsett in NJ

Approximately 150 gal ±5 (0.57 m^3) was discharged into each test hoop. This translates to an average film thickness if the oil were distributed evenly over a perfectly uniform ice sheet of 3.6 cm. In reality, the ice thickness is not completely uniform and there are localized areas of thick and thin oil films as well as patches with no oil within the test areas. Similar irregular distributions were observed in previous experiments where oil was spilled under ice into skirted areas (e.g. Balaena Bay 1975, CRREL indoor test tank 2004, and Svalbard 2006).

The first day of GPR testing concentrated on collecting data over the encapsulated oil layer, within the still uncontaminated skirt (as a control) and over clean undisturbed ice between the two skirts. This data established a baseline of ice/water interface reflection data and documented any localized skirt interference that needed to be considered in interpreting the later results.

Following these initial baseline tests, oil was injected under the remaining clean skirt (Hoop #2) and testing continued through the remainder of the four-day test window to test the performance of both new radar systems as well as an existing commercial system manufactured by Sensors and Software (similar the system used operationally by Alaska Clean Seas in Prudhoe Bay and tested previously at CRREL and on Svalbard.

4. Ice Sheet Growth and Properties

4.1 Thickness and Temperature

CRREL began growing the ice sheet on December 23, 2010. The initial aim of achieving a final thickness between 1.3 and 1.5 m by late February had to be downgraded to "close to one meter") after the initial freezing was delayed by unusually warm temperatures at the end of 2010. **Fig. 7** shows the ice growth curve leading to a final average thickness of 92 cm by the beginning of March.

During the test week the temperatures in the upper 30-40 cm of the sheet were sensitive to diurnal swings in air temperature, due to the lack of any snow to insulate the ice and strong solar absorption during the daytime with the roof pulled back. **Figs. 8 and 9** show the air and internal ice temperatures during the growth and test phases. Periods with the roof pulled back, exposing the ice to ambient conditions show clearly as a rapid increase in ice temperatures.

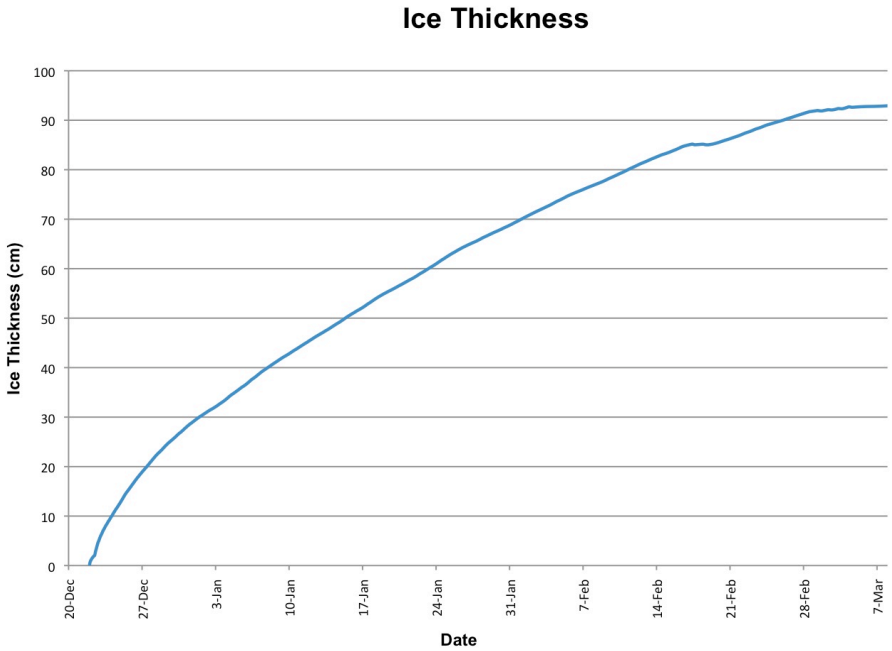

Figure 7. Ice thickness curve from freeze-up Dec 23/10 to early March 2011

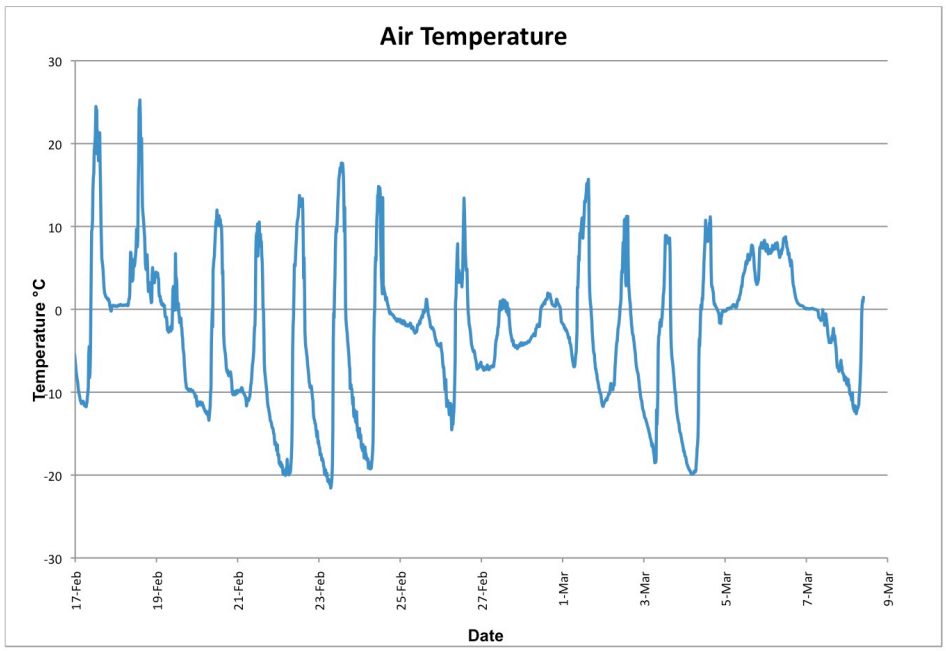

Figure 8. Air temperatures at CRREL (vicinity of the tank) from just before conducting the first spill on February 18 to March 9. Note the sharp diurnal fluctuation during the test week from March 1-4.

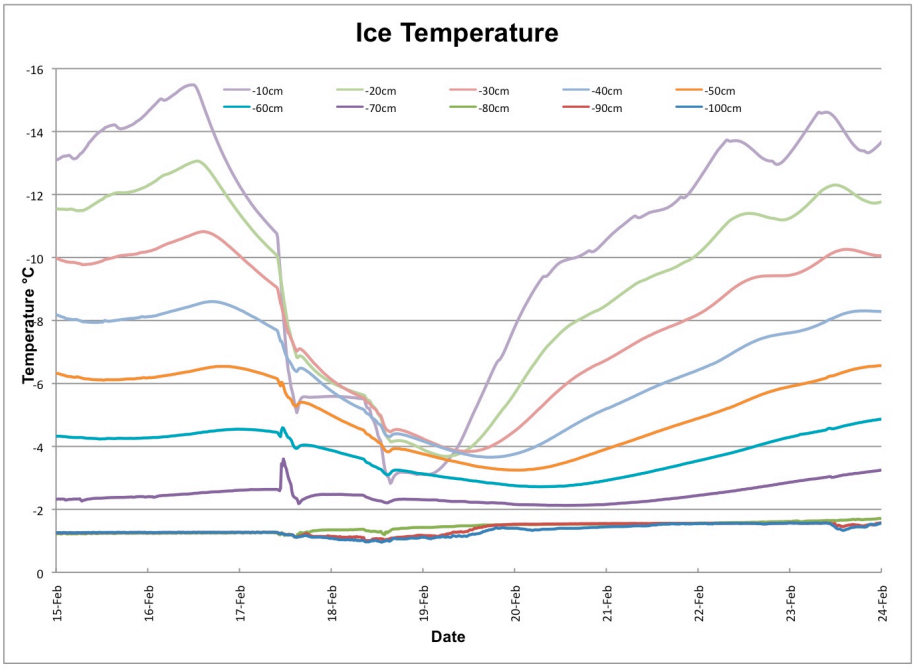

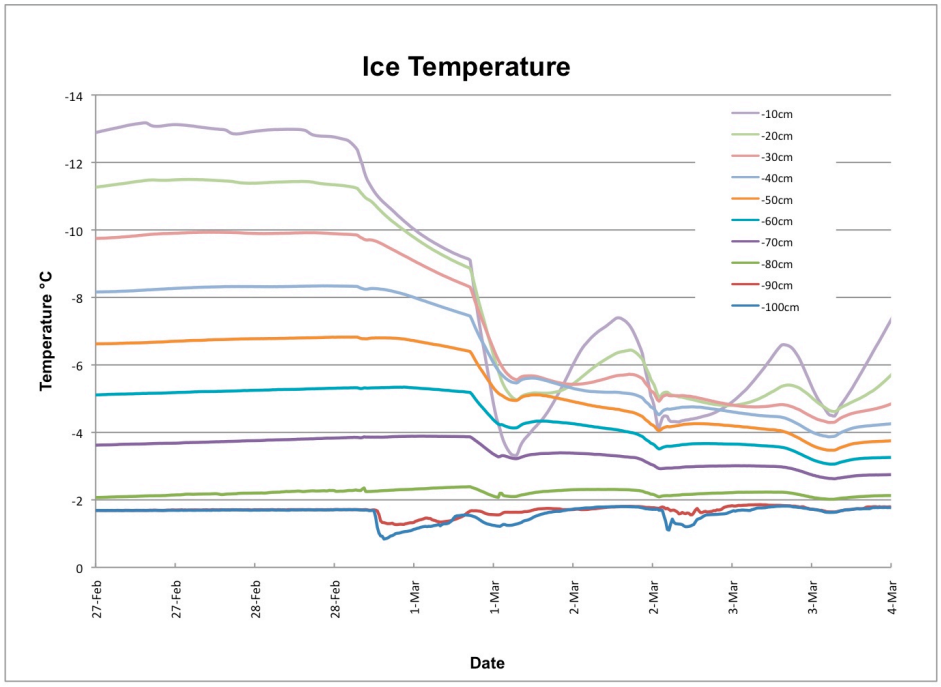

Figure 9. Internal ice temperatures at 10 cm intervals from top to bottom. Note: readings at 90 and 100 cm correspond to the water temperature at or immediately below the ice. Once the refrigeration was turned off on March 1 and the roof rolled back, temperatures in the upper 40-50 cm of the sheet rapidly increased, with the entire ice sheet becoming warmer than -6°C, except for diurnal swings in the upper 20 cm in response to colder nights.

4.2 Ice Coring and Drilling Results

On the last test day, May 4, following completion of the radar surveys, CRREL personnel documented the ice properties (temperature and salinity), ice thickness, oil thickness (Hoop #1 only) and oil distribution through a series of cores and drill holes. Oil thickness could only be determined directly for the first spill where enough time had elapsed to form a hard new ice layer beneath the oil. This meant that when a hole was drilled completely through the sheet it was possible to detect the bottom of the parent ice (at the time of the spill) and the top of the new ice layer, thereby measuring the depth of the oil layer. In both hoops it was possible to clearly distinguish between drill holes encountering oil and those that did not. This served to delineate several broad areas where no oil accumulated, for example under the south corners of Hoop #2. **Figs. 10 to 13** show the results presented as contour plots from the ice thickness profiles within each of the test areas.

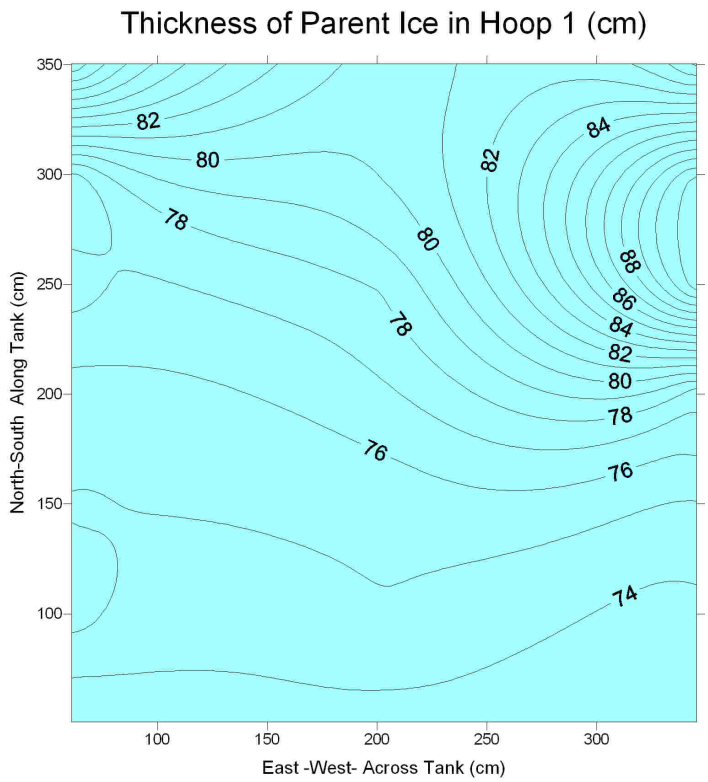

Figure 10

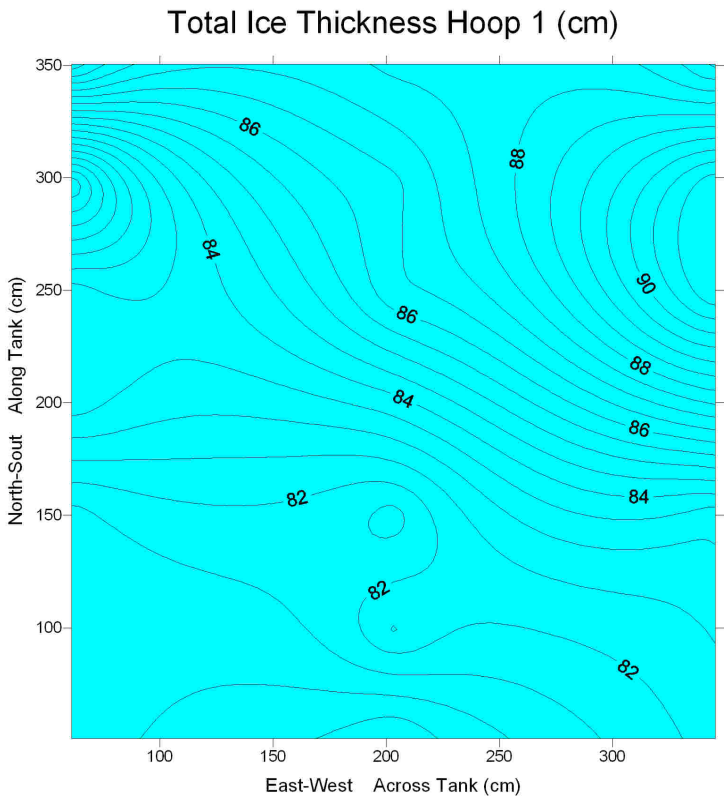

Figure 11.

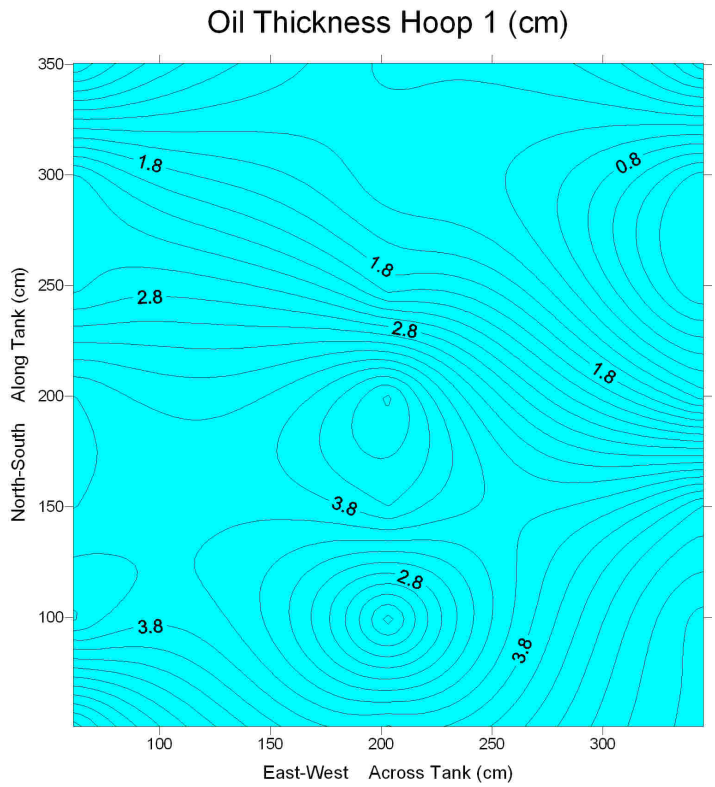

Figure 12.

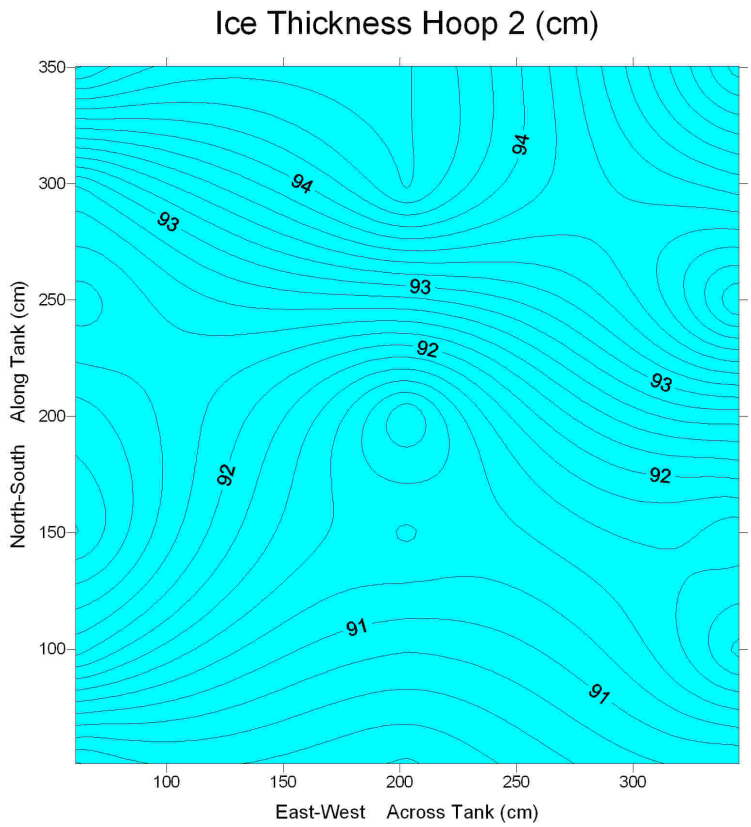

Figure 13.

Figure 14. Taking the second of two cores extracted for salinity and temperature in the clean ice between the two test hoops. See results below in **Fig. 18**

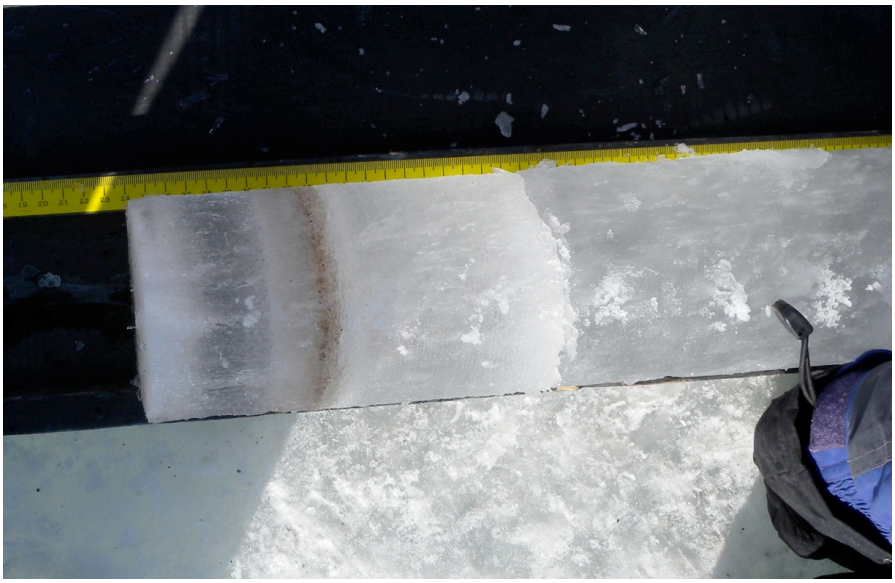

Figure 15. Band of fine oil droplets (< 1mm) 9 cm from the bottom of the cores through clean ice. This indicates that a very small % of the oil pumped in the first discharge was sheared into droplets at the point of exiting the hose. These droplets then drifted laterally beyond the skirt boundaries before rising to become incorporated in the growing ice interface.

Figure 16. Bottom of a core extracted on March 4 from within Hoop #1. There was a hard layer of new ice formed beneath the oil but this was lost in extracting the core. Some migration of oil through the porous skeletal layer making up the bottom 7-10 cm is visible internally within the core as oiled filled brine channels. The small pockets of contamination higher up are an artifact of the coring through oil and subsequent cleaning.

Figure 17. Logging the internal core temperature with a thermistor probe before slicing into sections for melting and subsequent salinity measurement (Fig. 18)

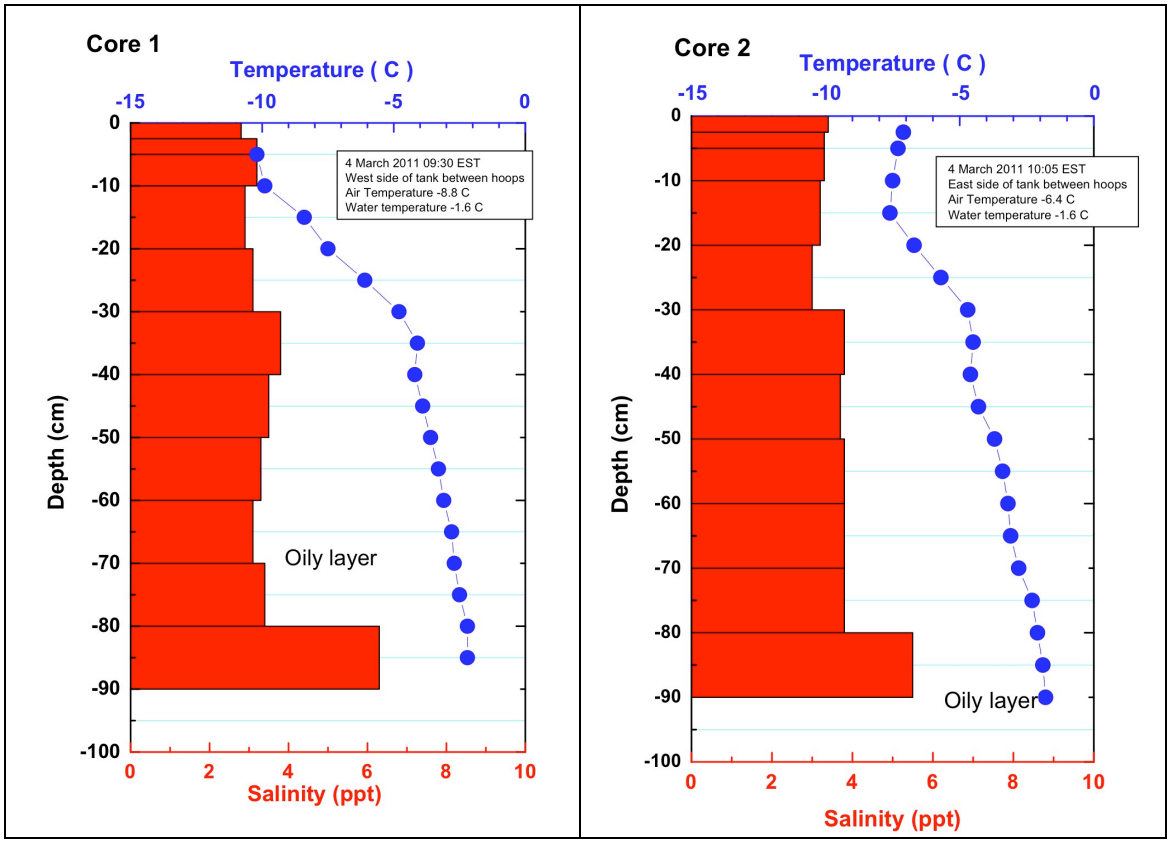

Figure 18. Salinity and temperature profiles from the ice cores.

5. Radar Data Interpretation

Three radars were subjected to comparison testing from the surface and suspended from the moving gantry: the two new systems built for this project using horn and parabolic reflector antennae and a third commercial system similar to those used in past oil in-ice experiments (e.g. Svalbard 2006 and 2008).

Overview: The pulse radar operating at 500 MHz clearly mapped the oil presence and distribution in both cells from the surface (probably the most unambiguous data set acquired to date over 7 years of research) and also detected oil with an average thickness of 1.3 cm trapped in the lower few centimeters of an 84 cm (avg.) ice sheet while suspended from the gantry. The new frequency modulated continuous wave (FMCW) systems operating over the .5 to 3GHz range achieved one of the primary objectives of the new design approach by isolating the signal from interference with the gantry (and by inference the helicopter as well). However, the interpretation of the multiple reflections with either of the new antennae is not straightforward with the electronics that exist now. An analysis of the signal-to-noise ratio (SNR) and comparison with modeling results shows that there was no significant decrease in SNR caused by the gantry, which is an improvement over the less directional GPR. The SNR for the FMCW systems must be improved by a factor of approximately two in order to detect oil under ice. Major improvements are currently underway to achieve this goal, which is now well defined.

Fig. 19 shows the two test hoops in a view from the top of the gantry. Measurements were being conducted at the time to acquire a profile of the ice resistivity along the full length of the tank.

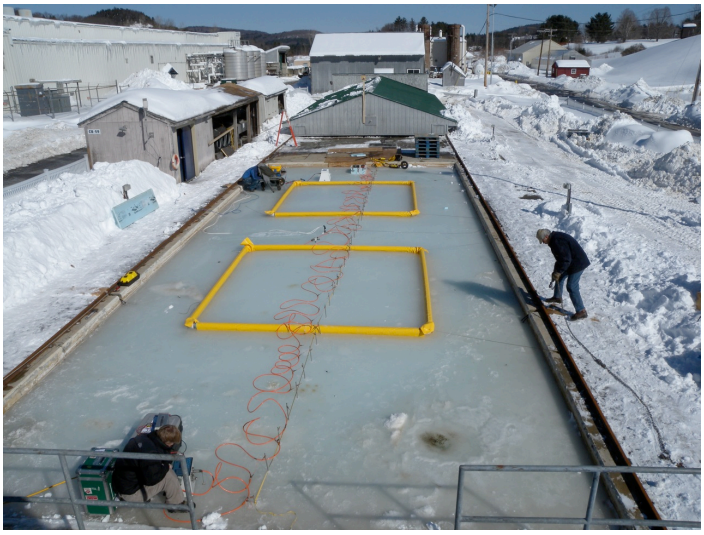

Figure 19. Overall view of the tank showing the two test hoops.

5.1 Commercial Radar Tests

The commercial radar was tested with both 1 GHz and 500 MHz pulsed antennas in ice-coupled mode (**Fig. 20**) and suspended approximately 3 m above the ice from the gantry. Both antennas performed well and were able to image the base of ice in both airborne and ground-coupled modes. Efforts focused on acquiring data along a centerline parallel to the long axis of the tank both before and after emplacement of the oil beneath Hoop 2. After the oil was emplaced, a 3D survey was completed in both ground coupled and airborne modes using the 500 MHz antennas. Finally, 4 sets of expanding spread gathers were acquired in each containment hoop, with 2 orthogonal polarizations parallel to both axes of the tank. These data enable electromagnetic velocity estimation and evaluation of offset dependent reflectivity anomalies.

Figure 20. Commercial radar being tested in ground-coupled mode

In interpreting the data, it is important to recognize two key physical properties of the ice in the test tank. First, the ice was observed to be strongly anisotropic. Anisotropy occurs in naturally growing sea ice where consistent currents in the underlying seawater cause the crystal structure of the ice to become preferentially aligned with the direction of flow. This alignment allows the film of brine that forms on the surface of the crystal to become connected in one direction, while being disconnected orthogonal to the primary crystal axis. Connectivity of the brine means that it forms a continuous conductor in one direction and the bulk ice conductivity appears high, while in the orthogonal direction, the bulk conductivity is low. The radar signal is strongly attenuated when the signal polarization is aligned with the connected brine film; in this case the reflection from the base of the ice may be weak or below the noise threshold. In the orthogonal direction, the signal undergoes little attenuation and a high-amplitude reflection from the base of the ice may be observed.

The ice in the test tank was not expected to be anisotropic, and the occurrence of strong anisotropy was surprising (**Fig. 21**). It is likely that weak convection currents were present in the brine while the ice was growing and that this produced an adequate current to preferentially align the ice crystals. The presence of the skirts altered the convection currents so that abrupt flow pattern boundaries were present at the hoop boundaries, therefore optimal orientation of the antennas depended on the position within the tank. Optimal orientation along the centerline varied as follows:

1) Polarization perpendicular to the tank axis was optimal outside of the hoops - this orientation was used for the majority of ground-coupled surveys.
2) Polarization parallel to the tank axis was optimal within the Hoop 2 – this orientation was used for all gantry surveys.
3) The ice in Hoop 1 was either isotropic or the axis oblique to the tank axis since there was little variation in the radar response between the two orthogonal polarizations.
4) There was not adequate time to acquire all datasets with both polarizations since the focus was on the new radar systems. However, a cross pole system such as that configured for Alaska Clean Seas would have eliminated any issues associated with the anisotropy.

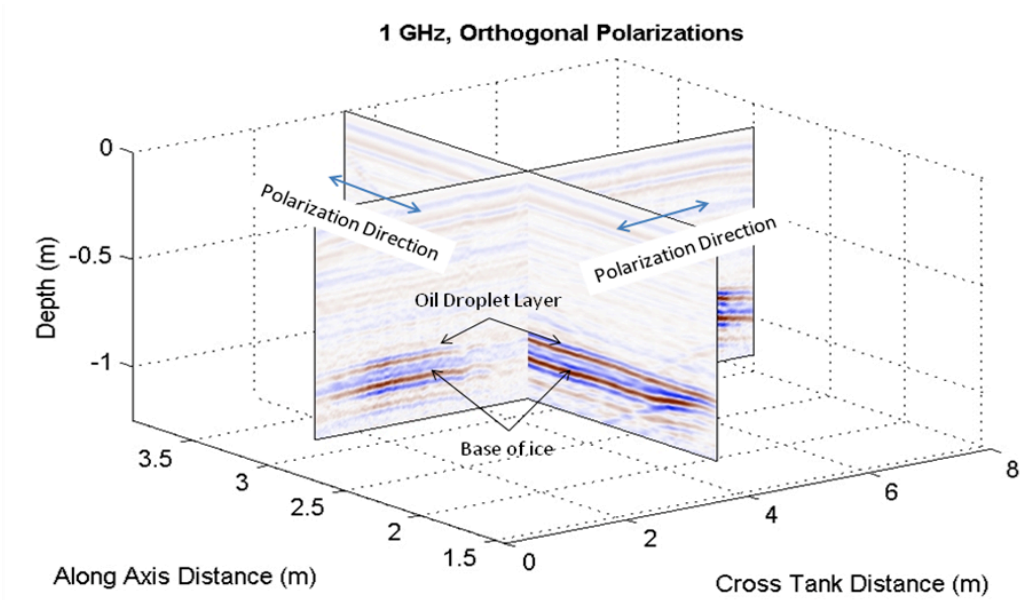

Figure 21. Ground coupled, 1GHz profiles with orthogonal polarizations acquired outside of the skirted areas and crossing south of Hoop 2. At this location, the polarization perpendicular to the tank axis is optimal along the centerline. Along the cross-tank line the crystal axis changes along profile; the antenna is optimally aligned near the edges but the signal is strongly attenuated near the center. Where the lines intersect, the base of ice reflection amplitude on the cross-tank profile drops to zero while reflection amplitude in the along axis profile remains high. The striking difference in amplitude at the intersection point indicates strong anisotropy.

The second physical property affecting interpretation of the data is the dynamic ice conditions that occurred during the experiment. As shown in Fig. 7, the ice warmed substantially from the first day of acquisition on February 28 to the final day of acquisition on March 4. The brine volume in the ice increases with increasing temperature, and the bulk electric conductivity of the ice increases with increasing brine volume. The net effect in terms of radar imaging is that signal penetration decreases with increasing temperature due to increased signal attenuation. During the CRREL test, the increase in temperature did not prevent the signal from reaching the base of ice, but we did note a decrease in the signal to noise ratio.

The relatively warm and anisotropic ice conditions combined to make this test more challenging and perhaps closer to field conditions than the 2004 tank test at CRREL. Particularly challenging was the anisotropy and lack of orthogonally polarized data. These factors must be taken into account in the interpretation.

5.1.1 Ground coupled profiling

Comparing the 500 MHz, ground-coupled profiles before and after the oil was emplaced in Hoop 2 (**Fig. 22)**, we see:

1) The effect of anisotropy is evident as the amplitude of the base of ice reflection decreases dramatically in Hoop 2.
2) The entrapped oil layer in Hoop 1 is clearly evident as a high amplitude anomaly.
3) There is a substantial increase in the base of ice reflection in Hoop 2 after the oil is pumped in.

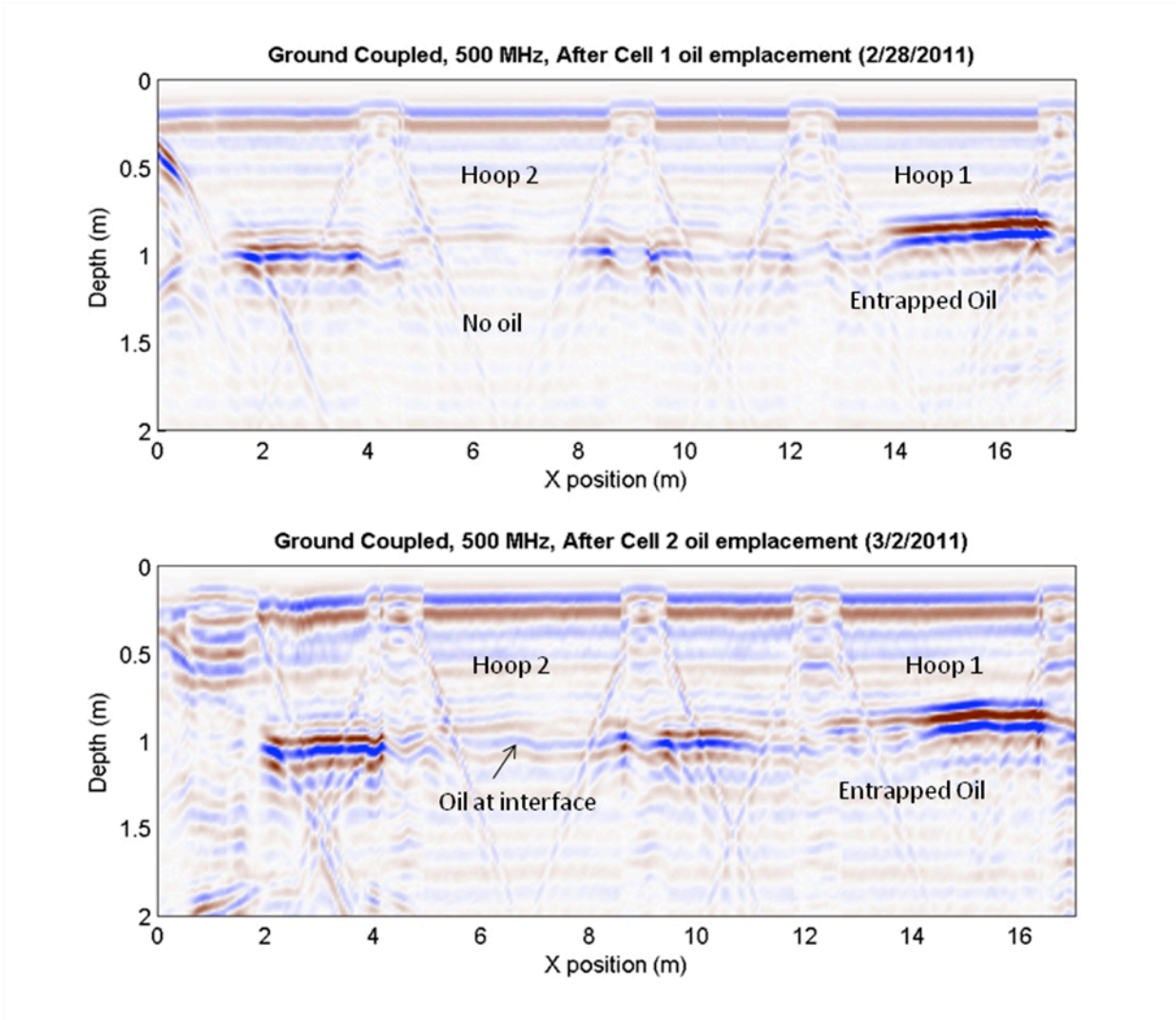

Figure 22. Comparison of ground-coupled, 500 MHz profiles beofore and after oil emplacement in Hoop 2. There is a large amplitude increase of the base-of-ice reflection in Hoop 2 after oil emplacement, although the reflection strength remains lower than that in the surrounding ice due to suboptimal polarization alignment.

The reflection strength, instantaneous frequency, and instantaneous phase attributes for the profile after oil was emplaced in Hoop 2 show a clear anomaly over the entrapped oil in Hoop 1, but give no clear indication of the oil in Hoop 2 (**Fig. 23**).

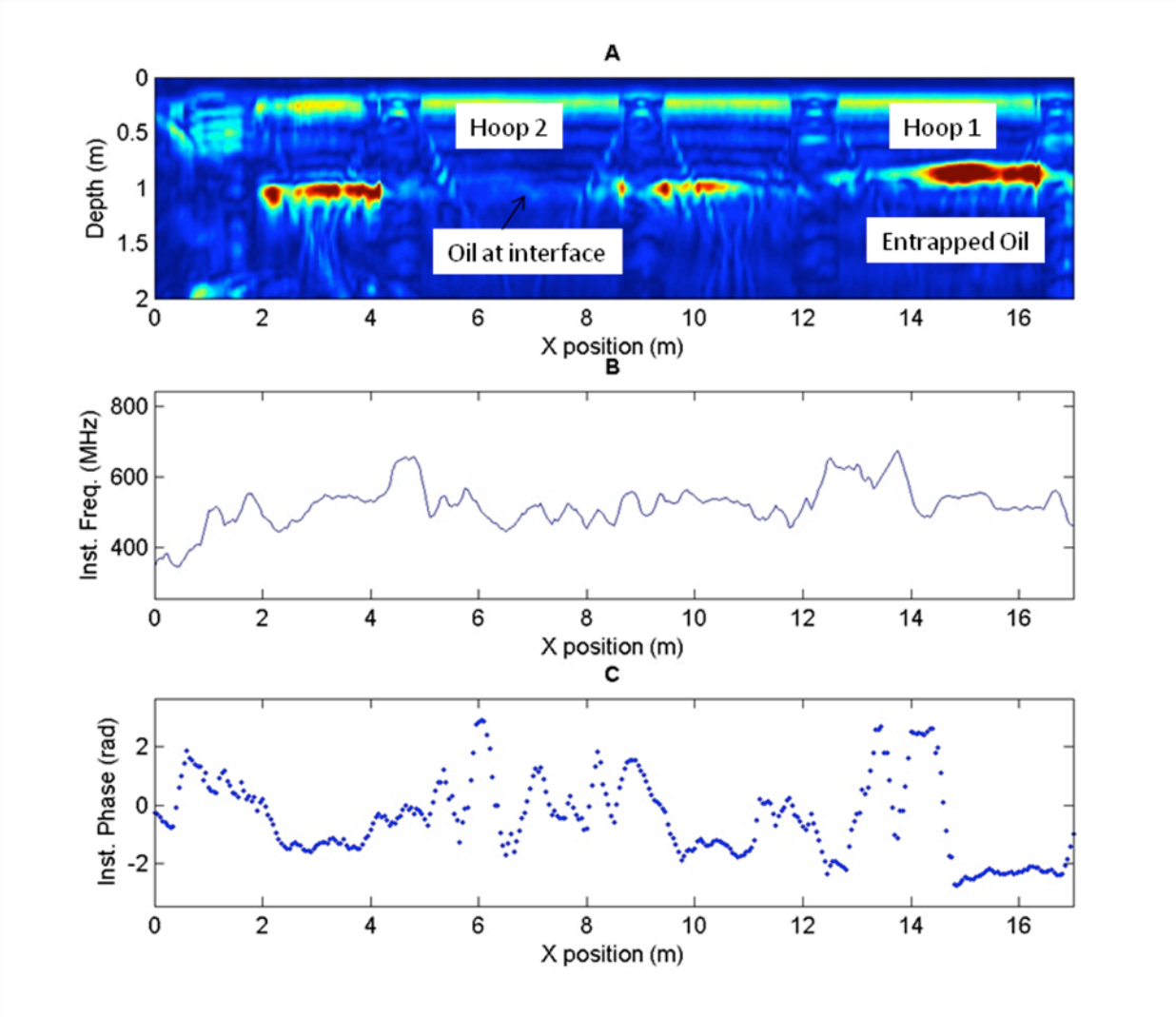

Figure 23. Instantaneous attributes taken from the ground-coupled 500 MHz profile after oil emplacement in Hoop 2. A clear amplitude and phase anomaly are present over the entrapped oil in Hoop 1 but there is no clear differentiation of oil in Hoop 2 because of anisotropy.

An orthogonal profile was acquired over Hoop 2 after oil emplacement **(Fig. 24)**. The polarization of this profile has optimal alignment with the ice anisotropy and shows a clear, high-amplitude reflection from the base of the ice across the entire profile. Reflection attributes extracted from this profile clearly differentiate the oiled area from that outside of the skirt as an increase in reflection amplitude, increase in instantaneous frequency, and decrease in instantaneous phase (**Fig. 25**). These changes are consistent with the modeled response based on measured ice salinity and temperature, and the expected mean oil thickness of 3.6 cm (see modeling section below).

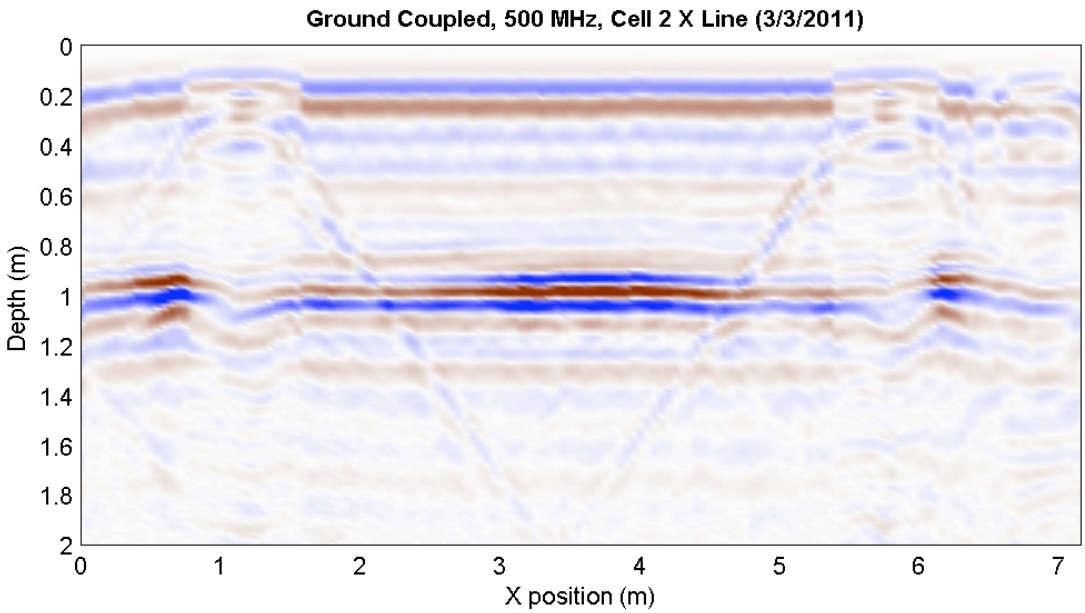

Figure 24. Cross tank profile with optimal antenna polarization. The base of ice is clearly evident over the entire profile with the reflection onset occuring at a depth of just over 90 cm. The reflection from the entrapped oil film is evident as a weak reflection with onset at around 83 cm.

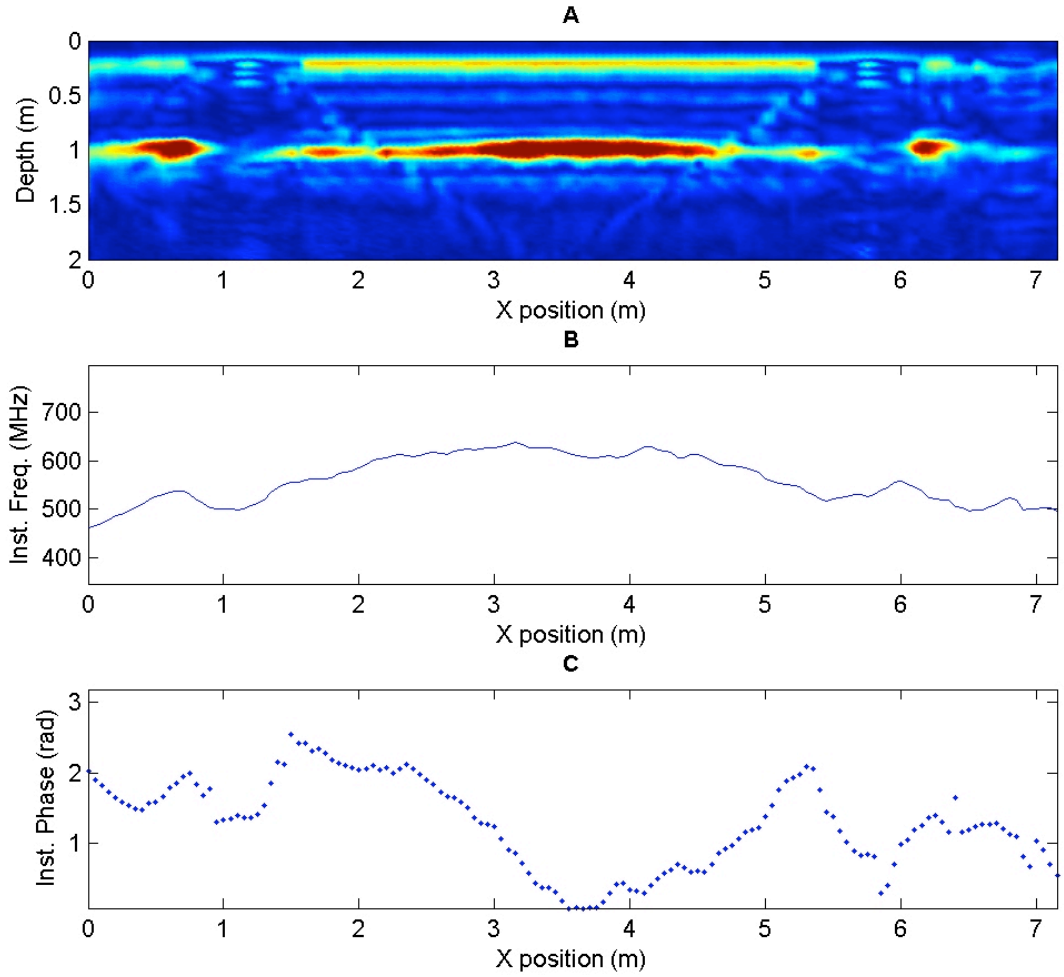

Figure 25. Reflection attributes extracted from the cross tank profile over Hoop 2 clearly differentiate the oiled area with an increase in reflection amplitude, increase in instantaneous frequency, and decrease in instantaneous phase.

5.1.2 Off-ice profiling

In all cases of off-ice profiling to simulate an airborne application, the radar antennas were suspended approximately 3 m above of the ice, and polarization was oriented parallel to the long axis of the tank. This polarization was optimal for imaging within the two hoops but not effective for imaging outside the skirted areas. This polarization was consistent with the orientation of the new radars. A substantial amount of coherent noise was recorded that was related to the antennas relative lack of directionality and proximity to the gantry beam. Multiple reflections from the gantry, field coupling with the gantry, and out of plane reflections from the antennas cables, GPR operator, and objects on the side of the tank resulted in an exceptionally noisy environment with a signal to noise ratio of less than 0.5 at the base of ice target reflection (**Fig. 26A).** This level of noise is higher than we have observed with the same system deployed from a

helicopter. The target reflections were successfully extracted in two processing steps: 1) Laterally coherent noise was attenuated using a median background subtraction (**Fig. 26B**) and 2) the scattered energy was collapsed to the point of origin using wavefield migration (**Fig. 26C**). This latter step produces some artifacts that appear as upturned arcs. The artifacts are related to inexact positioning of traces and reflected energy that violates the 2D assumption of the particular algorithm that was applied.

In comparing the images before and after oil emplacement, it is important to recognize that the ice temperature warmed substantially during this intervening time and because of this, substantial differences are expected. Nevertheless, in both cases, the base of ice reflection is clearly imaged within the skirted areas (**Fig 27**). And, as with the cross-tank profile, a substantial phase rotation occurs when the oil is present at the ice water interface.

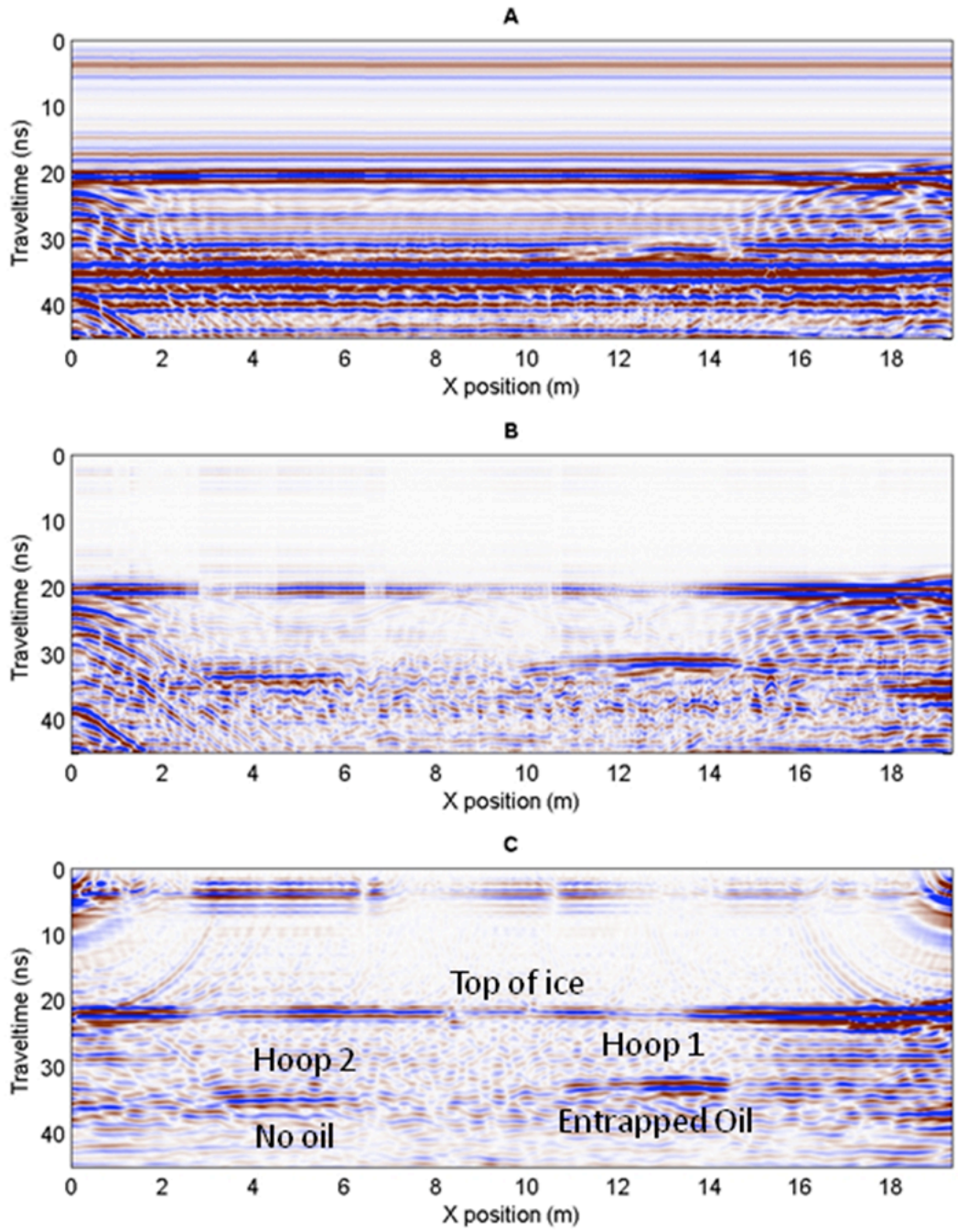

Figure 26. 500 MHz centerline profiles, suspended from gantry ~ 3m above the ice. A) Raw data, B) Data with median background subtraction, C) Data after wavefield migration.

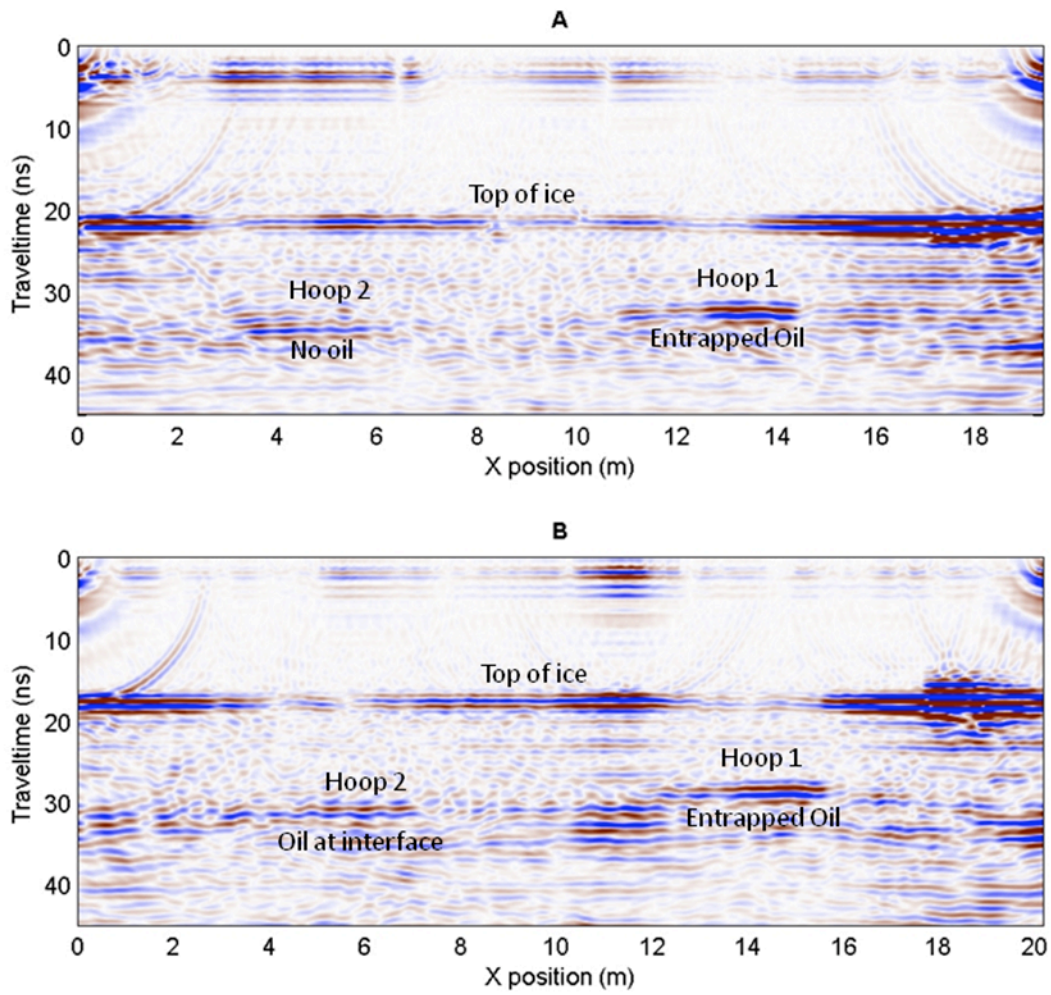

Figure 27. A) Off-ice centerline profile before Hoop 2 oil injection, and B) after oil injection. While coherent noise was attenuated, the processed images have substantially lower signal to noise ratios than the ground-coupled images. Despite this problem, the base of ice is well imaged within the two containment hoops. In Hoop 2, there is a clear phase rotation and amplitude increase that occurs after oil is placed at the ice/water interface.

5.1.3 Expanding spread gathers

Expanding spread gathers are acquired by moving the source and receiver away from a common center point at regular spatial intervals. As the distance between the source and receiver increases, the time it takes a wave to travel from the source, to a reflector, and back to the receiver increases. The change in travel time with increasing offset can be used to measure the velocity with which the wave is traveling and in turn, the velocity can be used to measure the depth to a given reflector.

Additionally, the angle at which the wave strikes a reflector increases as the source-receiver offset increases. Changes in reflection amplitude as a function of angle of incidence provide additional material property information such as oil layer thickness and dielectric permittivity.

After the completion of all other radar activities, we acquired 4 sets of expanding spread gathers in each of the containment hoops. The gathers included data in orthogonal polarizations about two separate midpoint locations – one near the skirt and one approximately 1.5 m toward the center of the skirt. The expanding spread gathers have high signal to noise ratios and enable accurate estimation of the bulk radar wave velocity (**Fig. 28**).

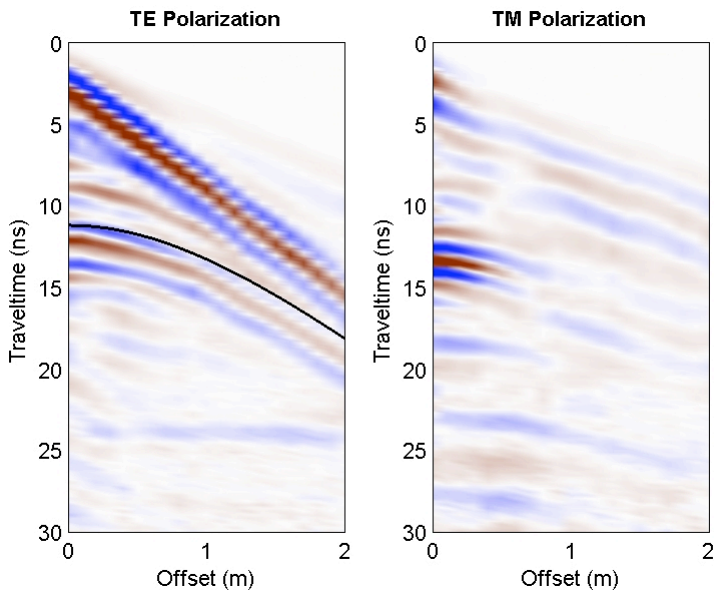

Figure 28. Expanding spread gathers acquired over Hoop 2 with polarization perpendicular (TE) and parallel (TM) to the long axis of the tank. The black solid line shows the curve for a bulk velocity of 0.142 m/ns, which is consistent with expected values based on ice temperature and salinity. Variations in amplitude with polarization and offset can help characterize material thickness and permittivity.

5.1.4 Modeling

The ice temperature and salinity measured in two ice cores on March 4 were used with the model developed in a previous phase of this project to estimate electromagnetic properties of the ice (**Fig. 29**) and the radar response with and without a 3 cm thick oil layer at the base of the ice (**Fig. 30**). Note that for modeling, a 1 cm thick layer with properties representative of an oil sheen was placed 8 cm above the base of the ice to simulate the thin entrapped layer of fine oil drops that appears to have been present throughout the tank. This thin layer was likely deposited by a small accidental release that occurred while emplacing the entrapped oil layer in Hoop 1 (**Fig. 15**).

There is excellent agreement between modeled and field traces taken from the cross-tank profile shown in Figure **24**. The model correctly predicts relative changes in phase (wavelet shape), frequency content, and amplitude that occur when an oil layer is present at the ice water interface. Further, the modeled electromagnetic properties are within measurement error of all field measurements. These results provide further evidence that the developed modeling tools can accurately predict the field radar response given inputs of ice temperature, salinity, and oil permittivity.

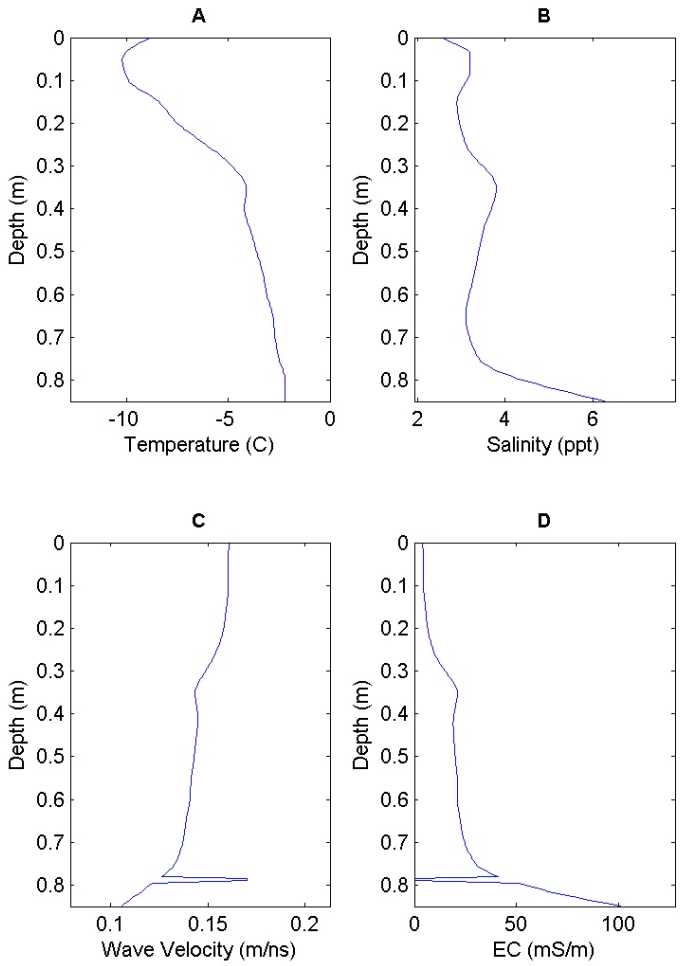

Figure 29. A) Temperature and B) salinity measured from ice cores on March 4. C) Electromagnetic wave velocity, and D) electric conductivity computed from A and B using the property model developed during a previous phase of this project. Note the spike at 0.78 m that corresponds to the depth of the thin entrapped oil sheen observed throughout the tank.

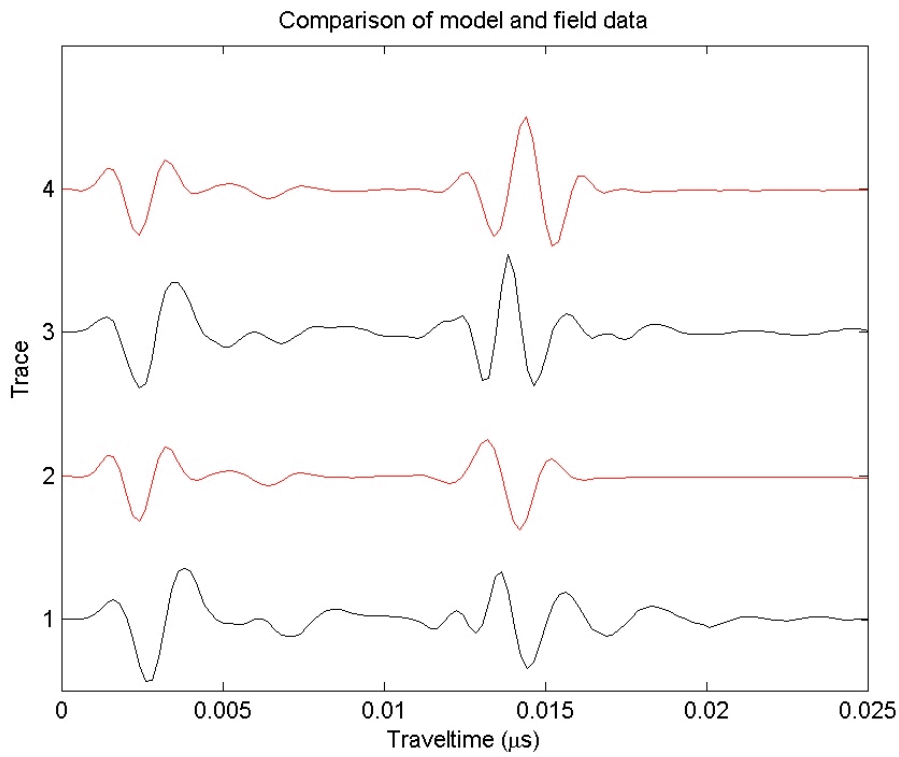

Figure 30. Model traces (red) and field data traces (blue) taken from the profile shown in **Fig. 24.** Traces 1 and 2 have no oil, and traces 3 and 4 have 3 cm of oil at the base of the ice. Note that 3.6 cm is the average expected oil thickness based on the known area and volume of oil. This parameter was not measured in the field.

5.2 FMCW radar results

Figs. 31 to 34 show the two new FMCW radar systems developed for this project and activities during their testing at CRREL.

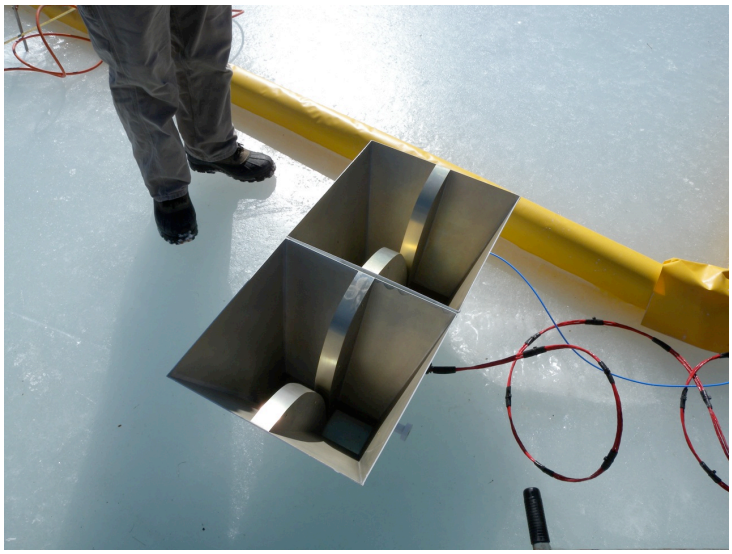

Figure 31. View of the horn antennae inverted to show the wave-guides designed to allow a wide band-width (frequency range).

Figure 32. Testing the horn antenna in an ice-coupled mode.

Figure 33. Suspending the horn antenna beneath the gantry frame.

Figure 34. Parabolic antenna mounted on the gantry.

5.2.1 Experiments on the ice surface

The CRREL experiments represent the first field tests for both the horn and parabolic reflector dish radar systems after 1 year of development and fabrication. Initial tests were performed over the ice in which the radar system was placed on the ice surface, and then raised up and lowered back down to the surface by hand. This experiment allows confirmation that the radar system is working, as reflections caused by the ice will change location, while noise occurring due to reflections within the radar hardware will remain constant. **Fig. 35** shows the results of such an experiment, with returned power (the square of amplitude) shown as a function of travel time and trace number.

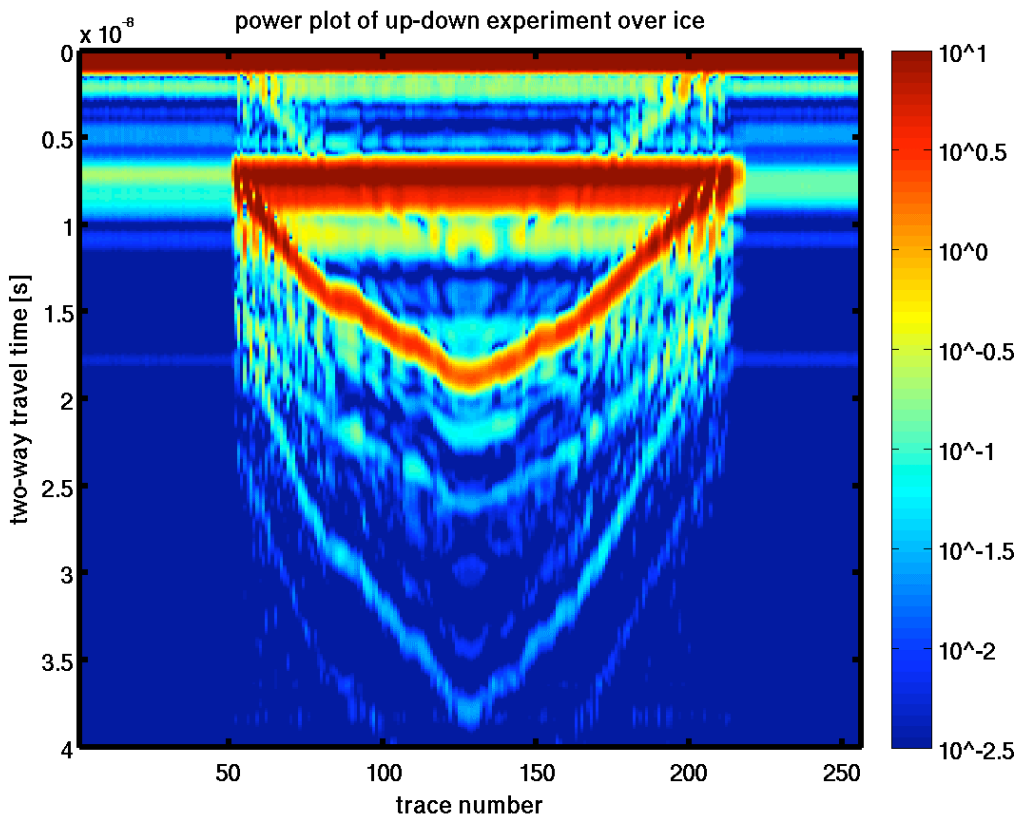

Figure 35. Up-down experiment over ice tank. Red reflection, which changes location, is caused by the ice surface. Various multiples are also shown.

The strong red reflection which changes location from 0.7x10^-8 seconds to 2 x10^-8 seconds is the ice surface. The deepest reflection, which changes location from the ice surface during the experiment, is clearly a multiple reflection. The reflection that parallels the ice surface was initially interpreted as the ice bottom while in the field. Upon subsequent careful analysis, this reflection remains at a constant travel time from the ice surface throughout all profiles, and therefore must be related to an internal multiple, likely caused by reflected signals entering the transmitting antenna. Future improvements will remove these signal artifacts.

5.2.2 Experiments on the gantry

A similar up-down experiment was performed with the horn antennas underneath the gantry, from the point of attachment, and the horns were lowered slightly to conclusively determine constant internal hardware noise from ice signals. An example of this type of experiment is shown in **Fig. 36**.

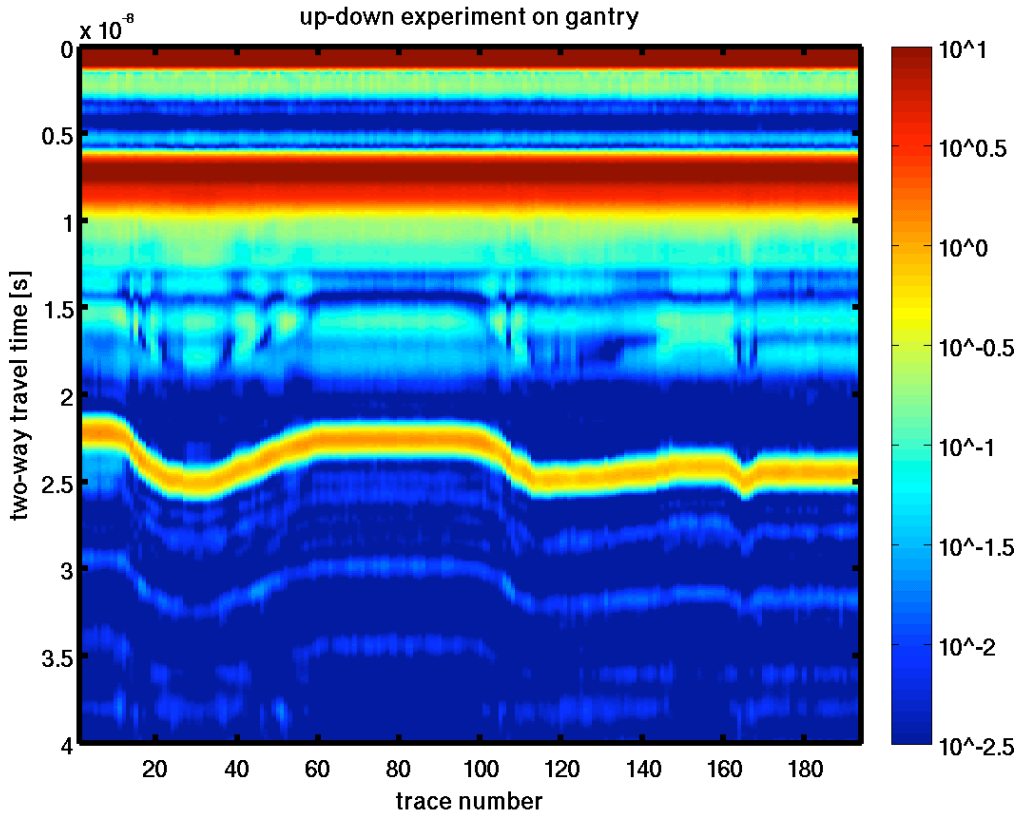

Figure 36. Up-down experiment from point of attachment on the gantry with the horn antenna FMCW system. Note the similar signal to noise ratio and the lack of additional artifacts caused by the gantry, due to the directional nature of this system.

This experiment indicated that when attached to the gantry, the noise level did not increase due to the directionality of the horn FMCW system. The ice surface reflection is the orange reflection between 2 and 2.5x10^{-8} seconds, which changes location during the experiment. Also seen is the parallel reflection about 8 ns below (3-3.2 x10^{-8} seconds) that appeared in the up-down experiment on the ice surface. The cause of this reflection is currently unknown, but likely due to reflected signals entering the transmitting antenna. Future hardware improvements planned are targeted to remove this type of signal artifact.

5.2.3 Signal to Noise ratio analysis

Understanding the differences in Signal to Noise Ratio (SNR) when operating from the surface and in the air with both the new FMCW system and the existing commercial system is critical to determining the SNR required to provide unambiguous detection of both the oil layer and the ice/water interface. The signal to noise ratio was calculated for all traces from both a surface and gantry mounted experiment, and the distribution of SNR for each are shown as separate box-plots in **Fig. 37**. SNR are calculated relative to the surface reflection. The box spans the middle 50% of the measurements, the red line is the median, and the whiskers span 99% of the data with outliers shown as red +'s. Note that the two distributions are not significantly different, and it appears that the directional nature of the horn antennas prevents reflections from the gantry from causing noise in the measurements. This confirms that the new designs have achieved one of the primary objectives, that of largely removing the influence of the helicopter as a noise source. However, the absolute SNR provided by the new system (as configured in the 2011 tests) fell short of that needed to detect the ice bottom and/or the oil layer.

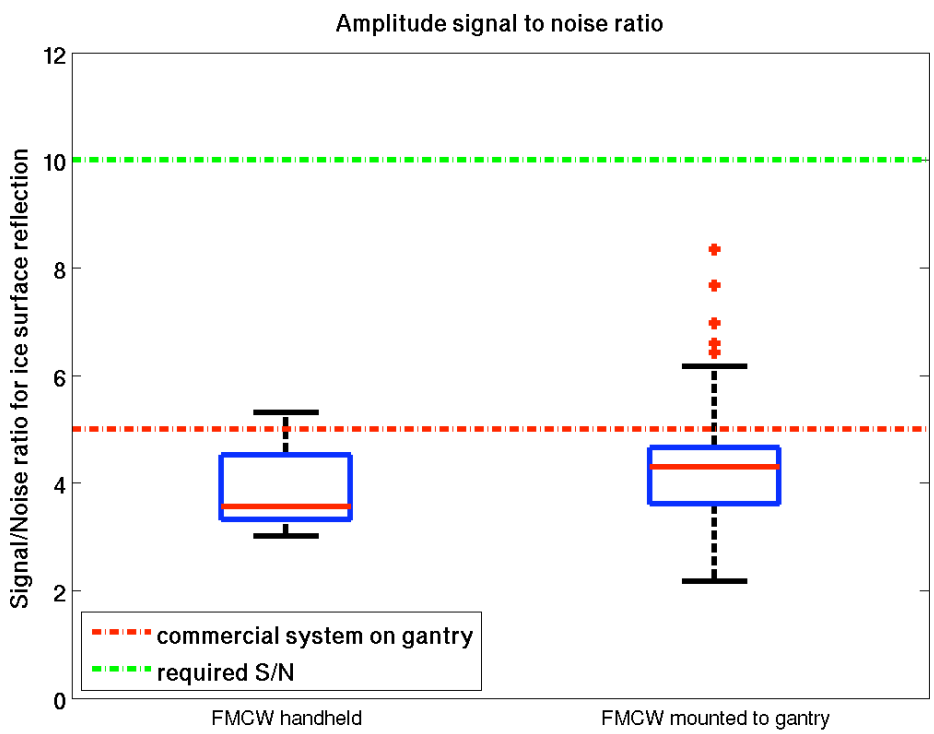

Figure 37:. SNR analysis for the FMCW horn-based system. The distribution from up-down measurements made at the ice surface is shown on the left, and when mounted to the gantry on the right. Note that there is no significant decrease in SNR when mounted to the gantry – one of the original objectives of developing the new systems with a much more focused transmitted signal. The dashed red line shows the SNR for the commercial system when on the gantry, and the dashed green line shows the required SNR needed to unambiguously detect oil underneath the ice, or the ice/water interface.

All signal-to-noise ratios were calculated based on the amplitude of the surface reflection relative to the largest amplitude noise near the target, which could possibly mask the oil or ice/water interface. All values are shown relative to the ice surface reflection, since this was detected with all systems. The FMCW horn system has on average a SNR lower than the commercial system when mounted on the gantry (shown in Fig. H3 as the red dashed line), which is why this new system was unable to detect the oil or ice/water interface. With the commercial system, it was possible to detect the oil even when operating ~3 m off the ice surface - after post-processing. The goal for the new hardware improvements (Section 6 and Attachment 1) is to achieve a SNR of 10 (shown in **Fig. 37** as the green dashed line), which would allow the oil and ice/water interface to be unambiguously detected, based on modeling results and GPR measurements explained above. Note that achieving this SNR of 10 for the ice surface reflection should allow detection of oil and ice/water interfaces when operating with the optimal orientation relative to the ice anisotropy. Therefore, at some point, an operational system will require to ability to acquire data in two orthogonal polarizations. This can be achieved either by doubling the antennae (increasing the challenge of obtaining flight permits), or alternatively using the onboard GPS to fly in orthogonal flight lines.

5.2.4 FMCW radar profiles from gantry

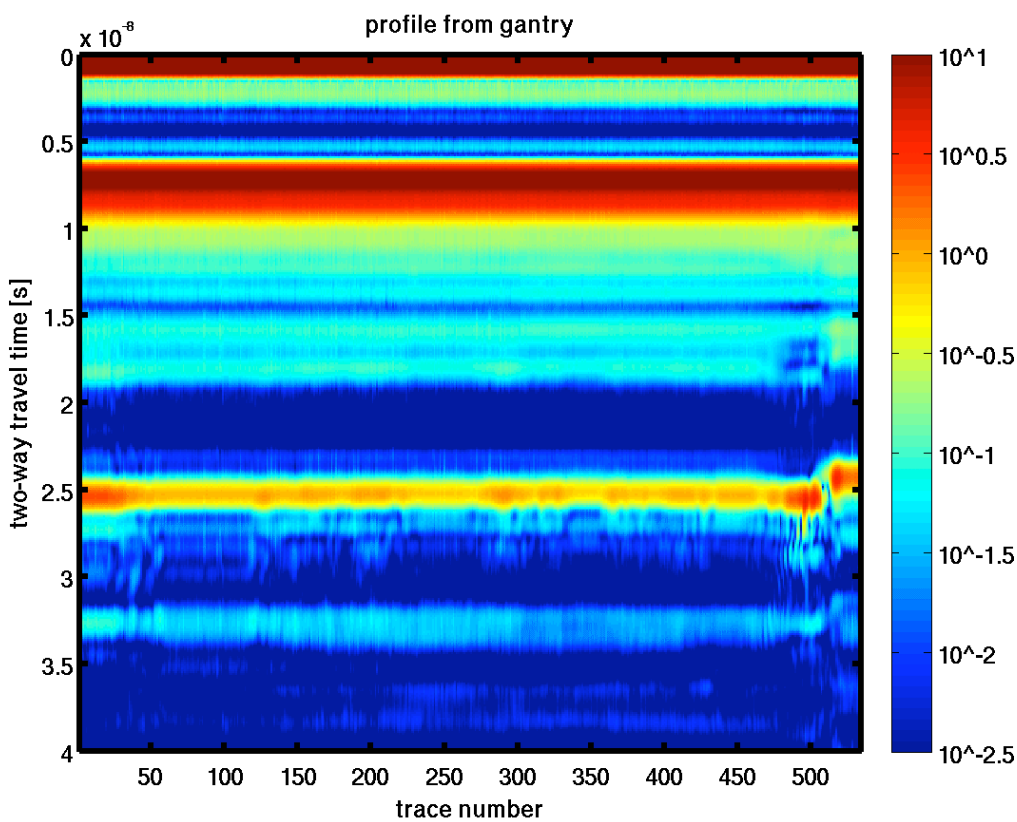

Figure 38. FMCW radar profile from gantry.

An example of FMCW radar profiles with the horn system suspended from the gantry along the length of the tank is shown in **Figs. 38 and 39.** Figure 38 shows the processed image with no background removal, and Figure 39 shows the same profile with the median trace removed, just as was done with the commercial GPR results shown above. Note that the surface reflection is located at 2.5x10^-8 seconds, and there is a second reflection at 8 ns below this (3.3x10^-8 seconds). In the field this appeared to be a possible ice bottom reflection, however, as you can see from this image the location from the surface reflection remains the same. Since we know the ice thickness did vary, this must be system-related noise. Figure 39 shows the location of Hoop #1 with entrapped oil between the white lines, and Hoop #2 with no oil between the green vertical lines. There are anomalous signals at approximately the correct location for the entrapped oil beneath Hoop #1, however these are at the same level or below the noise level and therefore we are not confident the current newly designed prototype systems are able to detect the presence of oil unambiguously.

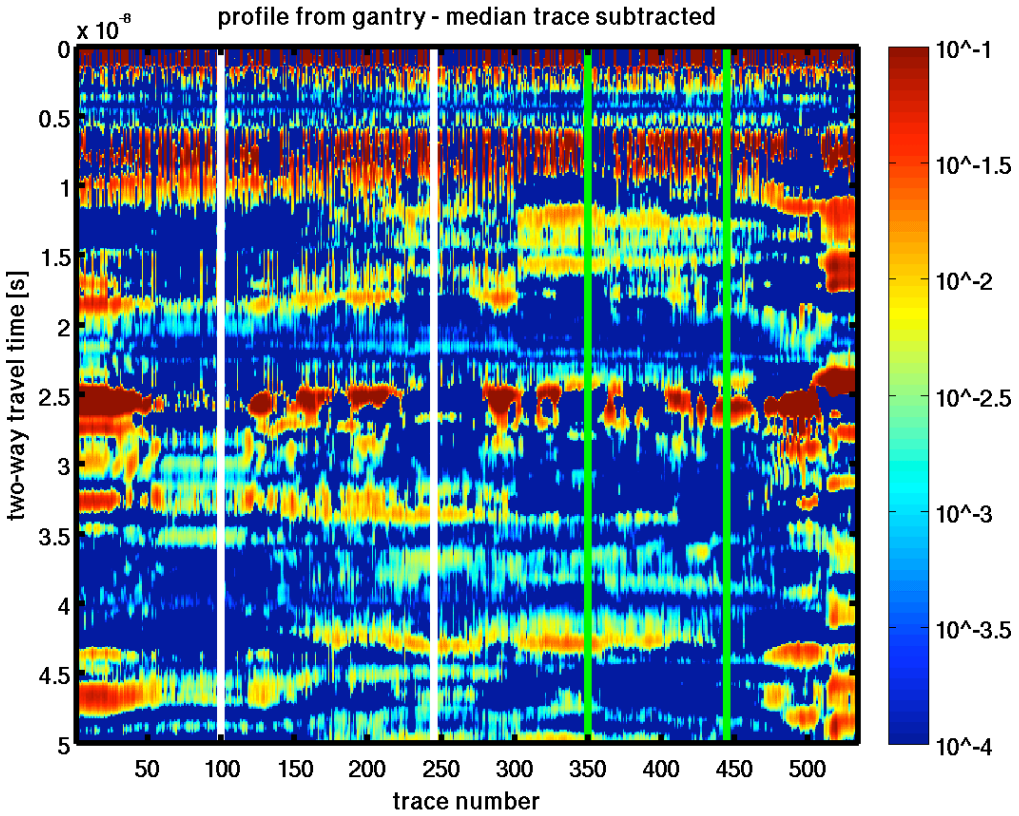

Figure 39. FMCW radar profile from gantry with background removed via a median trace filter.

6. 2011 Radar Design Improvements

As a direct result of the findings from the CRREL tests, the team proposed a number of steps to further develop and improve the new FMCW radar systems. The tests at CRREL were very useful in defining the new design objectives, especially in understanding the Signal to Noise Ratio (SNR) required to achieve a superior performance to the existing commercial impulse radar and ensure unambiguous detection of both the ice/water interface and any oil layers trapped beneath or within the ice (refer to **Fig. 37** and preceding discussion in Section 5.2.3). Although the absolute SNR achieved with the new radar as configured in early 2011 fell short of that required to achieve successful oil-under-ice detection, the tank tests showed that the increased directionality of the antennas prevented the Signal to Noise Ratio (SNR) from decreasing any further when attached to the gantry (a primary drawback to the existing commercial system). As a result there is increased confidence that minimal additional noise will result when the improved FMCW radar (see following and Attachment 1) is attached to a helicopter.

Specific recommendations made following the CRREL tests to improve the performance of the airborne radar together with the solutions implemented are summarized below:

a. **Phase-locked loop (PLL) -** to improve the phase stability of the oscillator. Unstable phase could be causing problems, especially at the lower frequencies. *This was accomplished by using a high-speed PLL designed specifically for swept FMCW systems.*

b. **Isolator.** This is a "one-way valve" that prevents signals from returning into the transmitting antenna and mixing with the received signal. *The new output gain stages will accomplish this in addition to providing additional transmit power for improved SNR.*

c. **Double-balanced mixer.** This would replace the current detector, and improve signal to noise ratio. *Done: In addition, the mixer was preceded by a low-noise amplifier to provide better SNR.*

d. **Higher frequency oscillator and frequency divider**. The original oscillator encountered problems at the low frequency range of most interest for oil under ice detection. *A different approach ended up being taken to solve this problem. In order to provide a continuous frequency sweep of 500 MHz to 2 GHz, the source was designed with a heterodyne approach of mixing two oscillators to yield the 2-octave range.*

Work to design and implement each these modifications was completed between June and December 2011. Attachment 1 contains a technical report describing the Design and Construction of the new FMCW System at Boise State University. The following extract from that report summarizes the overall design approach and target specifications that led to the current system.

6.1 Introduction

The purpose of this project is to develop a radar system with the goal of determining the presence of a relatively thin layer of oil under saline ice. A Frequency Modulated Continuous Wave (FMCW) architecture was requested because of the following benefits:

- Avoid the need to develop high-energy impulses associated with pulse radar
- Assure use of the maximum available spectrum to achieve the optimum distance resolution
- Operate at close range to the ice in order to achieve good spatial resolution. Pulsed radar minimum spacing is generally limited by the pulse width of the transmitted signal.

Due to the RF absorption of saline ice, it was determined that the upper frequency needed to be limited to 2 GHz. A lower frequency limit of 500 MHz was dictated by the bandwidth of the horn antennas. The inherent distance resolution of a radar system with 1.5 GHz bandwidth in air (ε_R=1) is 10 cm. This project will benefit from a somewhat higher ε_R but the challenge of achieving distance resolution on the order of a few cm is significant. The approach taken for this FMCW radar system is to optimize the design to develop the best possible capability to achieve the desired distance resolution by providing excellent control of the transmitted signal and optimized received signal quality with quadrature capability to enable the maximum opportunity to apply a variety of Digital Signal Processing (DSP) analysis methods.

6.2 Design Objectives

The resulting objectives of the hardware design for this FMCW system include:

- Operation over the frequency range of 500 MHz – 2 GHz
- Highly linear frequency sweep vs. time through the use of a synthesizer/PLL
- Capabilities to support sawtooth and triangular frequency sweeps as well as Frequency Shift Keying (FSK) operation
- Quadrature demodulation of the return signal
- Receiver noise figure of less than 3 dB
- Transmit power at least 10 dBm
- Receive channel compensation to provide some gain compensation for distance effects
- Operation from -40°C to 75°C
- Operation from +15V and +30V battery supplies
- Frequency control from 3 programmable digital outputs
- Three analog outputs: In-phase (I) and Quadrature (Q) channels and tuning voltage

6.3 Design Architecture and Construction

The design of the system is comprised of five independent modules. These are:

- Main Radio Frequency (RF) board, consisting of receiver and transmitter circuits (the largest module)
- Receiver LNA (Low Noise Amplifier)
- Transmitter PA (Power Amplifier)

- Synthesizer module which samples the transmitted RF signal and supplies the control signal to lock the Voltage Controlled Oscillators (VCOs)
- Power regulator module, which provides reduced voltages for the regulators on the other modules.

In order to optimize the receiver noise figure, a Low Noise Amplifier (LNA) module has been designed to mount directly to the receiver (Rx) antenna with the type N connector. This will avoid causing the cable losses from the antenna to add directly to the noise figure. A similar approach is used for the transmit antenna, where the power amplifier module is directly connected via a type N connector. There is adequate space in the vicinity of the transmit antenna for any necessary heat sinks, and the antenna itself could aid as a heat sink if desired. Both of the devices are relatively lightweight, so the connector should be able to support them even with relatively high vibration. This architecture allows for easy modifications to gains and output power, depending on the needs of the system.

> *Note: the transmitter will easily exceed Federal Communications Commission (FCC) limits for operation in the USA in a wide variety of bands, so for testing the device should be set to operate at powers that do not exceed these limits unless the testing is done inside a shielded chamber. For operation in other geographical areas, the power amplifier can be chosen to meet local requirements. Note that the frequencies emanating from this FMCW transmitter will interfere with devices using cell phone, GPS, and navigational frequencies.*

The initial approach considered for this project was to purchase packaged components that would be interconnected by RF coaxial cables and low frequency power and control signals. As the design evolved, it rapidly became clear that, to achieve the objectives, the approach of using interconnected modules would be impractical for several reasons.

- The number of components required would result in a very large and unwieldy solution.
- The implementation of a quadrature system requires very close matching of transmission line lengths to maintain the desired phase relationship – very difficult to do with discrete cables where the phase velocity is about 10 degrees/mm at 4 GHz.
- Some of the critical components are not commercially available in packaged form.
- The design of the system requires analog components to augment the performance of certain RF components in terms of tune control shaping for VCOs, bias control for various components, and variable gain controls.

For these reasons, the choice was made to use surface mount components applied to custom Printed Circuit (PC) boards to construct most of the required subsystems. The result of all of this optimization is a system that is significantly more complex than originally envisioned.

Attachment 1

Design and Construction of the Boise State University FMCW System.

Prepared by:

Robert Hay
rhay@allosys.com

AlloSys Corporation, Boise ID

December 17, 2011

1213 Kimberley Ln. Office 208-377-0246
Boise, ID 83712-7736 Mobile 208-850-5230
email rhay@allosys.com
Bob Hay President

Design and Construction of the Boise State University FMCW System.

Introduction

The purpose of this project is to develop a radar system with the goal of determining the presence of a relatively thin layer of oil under saline ice. An FMCW architecture was requested because of the following benefits:

- Avoid the need to develop high-energy impulses associated with pulse radar
- Assure use of the maximum available spectrum to achieve the optimum distance resolution
- Operate at close range to the ice in order to achieve good spatial resolution. Pulsed radar minimum spacing is generally limited by the pulse width of the transmitted signal.

Due to the RF absorption of saline ice, it was determined that the upper frequency needed to be limited to 2 GHz A lower frequency limit of 500 MHz was dictated by the bandwidth of the horn antennas. The inherent distance resolution of a radar system with 1.5 GHz bandwidth in air (ε_R=1) is 10 cm. This project will benefit from a somewhat higher ε_R but the challenge of achieving distance resolution on the order of a few cm is significant. The approach taken for this FMCW radar system is to optimize the design to develop the best possible capability to achieve the desired distance resolution by providing excellent control of the transmitted signal and optimized received signal quality with quadrature capability to enable the maximum opportunity to apply a variety of DSP analysis methods.

Objectives

The resulting objectives of the hardware design for this FMCW system include:

- Operation over the frequency range of 500 MHz – 2 GHz
- Highly linear frequency sweep vs. time through the use of a synthesizer/PLL
- Capabilities to support sawtooth and triangular frequency sweeps as well as FSK operation
- Quadrature demodulation of the return signal
- Receiver noise figure of less than 3 dB
- Transmit power at least 10 dBm
- Receive channel compensation to provide some gain compensation for distance effects
- Operation from -40°C to 75°C
- Operation from +15V and +30V battery supplies
- Frequency control from 3 programmable digital outputs
- Three analog outputs: I and Q channels and tuning voltage

Architecture

The design of the system is comprised of five independent modules. These are:

- Main RF board, consisting of receiver and transmitter circuits (the largest module)
- Receiver LNA (Low Noise Amplifier)
- Transmitter PA (Power Amplifier)
- Synthesizer module which samples the transmitted RF signal and supplies the control signal to lock the VCOs

- Power regulator module which provides reduced voltages for the regulators on the other modules.

In order to optimize the receiver noise figure, a LNA module has been designed to mount directly to the receiver (Rx) antenna with the type N connector. This will avoid causing the cable losses from the antenna to add directly to the noise figure. A similar approach is used for the transmit antenna, where the power amplifier module is directly connected via a type N connector. There is adequate space in the vicinity of the transmit antenna for any necessary heat sinks, and the antenna itself could aid as a heat sink if desired. Both of the devices are relatively light weight, so the connector should be able to support them even with relatively high vibration. This architecture, shown in Figure 1, allows for easy modifications to gains and output power, depending on the needs of the system.

Note that the transmitter will easily exceed FCC limits for operation in the USA in a wide variety of bands, so for testing the device should be set to operate at powers that do not exceed these limits unless the testing is done inside a shielded chamber. For operation in other geographical areas, the power amplifier can be chosen to meet local requirements. Note that the frequencies emanating from this FMCW transmitter will interfere with devices using cellphone, GPS, and navigational frequencies. The detector and AGC loop shown in the transmit antenna assembly is an optional future possibility and is not included in the current design.

The initial approach considered for this project was to purchase packaged components that would be interconnected by RF coaxial cables and low frequency power and control signals. As the design evolved, it rapidly became clear that, to achieve the objectives, the approach of using interconnected modules would be impractical for several reasons.

- The number of components required would result in a very large and unwieldy solution.
- The implementation of a quadrature system requires very close matching of transmission line lengths to maintain the desired phase relationship – very difficult to do with discrete cables where the phase velocity is about 10 degrees/mm at 4 GHz.
- Some of the critical components are not commercially available in packaged form.
- The design of the system requires analog components to augment the performance of certain RF components in terms of tune control shaping for VCOs, bias control for various components, and variable gain controls.

For these reasons, the choice was made to use surface mount components applied to custom PC boards to construct most of the required subsystems. The result of all of this optimization is a system that is significantly more complex than originally envisioned. This additional complexity will, unfortunately, result in a challenge to meet the original desired schedule. However, it is not anticipated that it will result in any cost implications.

The block diagram of the system is shown in Figure 1 Note that in this diagram (as well as in Figure 2), the predicted power level at each relevant RF node is shown in red and the DC power requirements (volts, mA) is shown in blue. The power amp design is still in flux due to more experimentation work needed to better define the power requirements and testing to better determine the available capabilities of the various options. The current implementation of the receive LNA stage includes only the single amplifier, pending more information on the received signal strength.

It is anticipated that there will be three physical shielded modules in this system

- the main module including the Rx and Tx signal systems, the synthesizer, and the power regulator
- the LNA (low noise amplifier) preamp connected to the receive antenna
- the PA (Power Amplifier) module connected to the transmit antenna

The main module can be attached to the antenna support structure in the space currently occupied by the electronics on the antenna system.

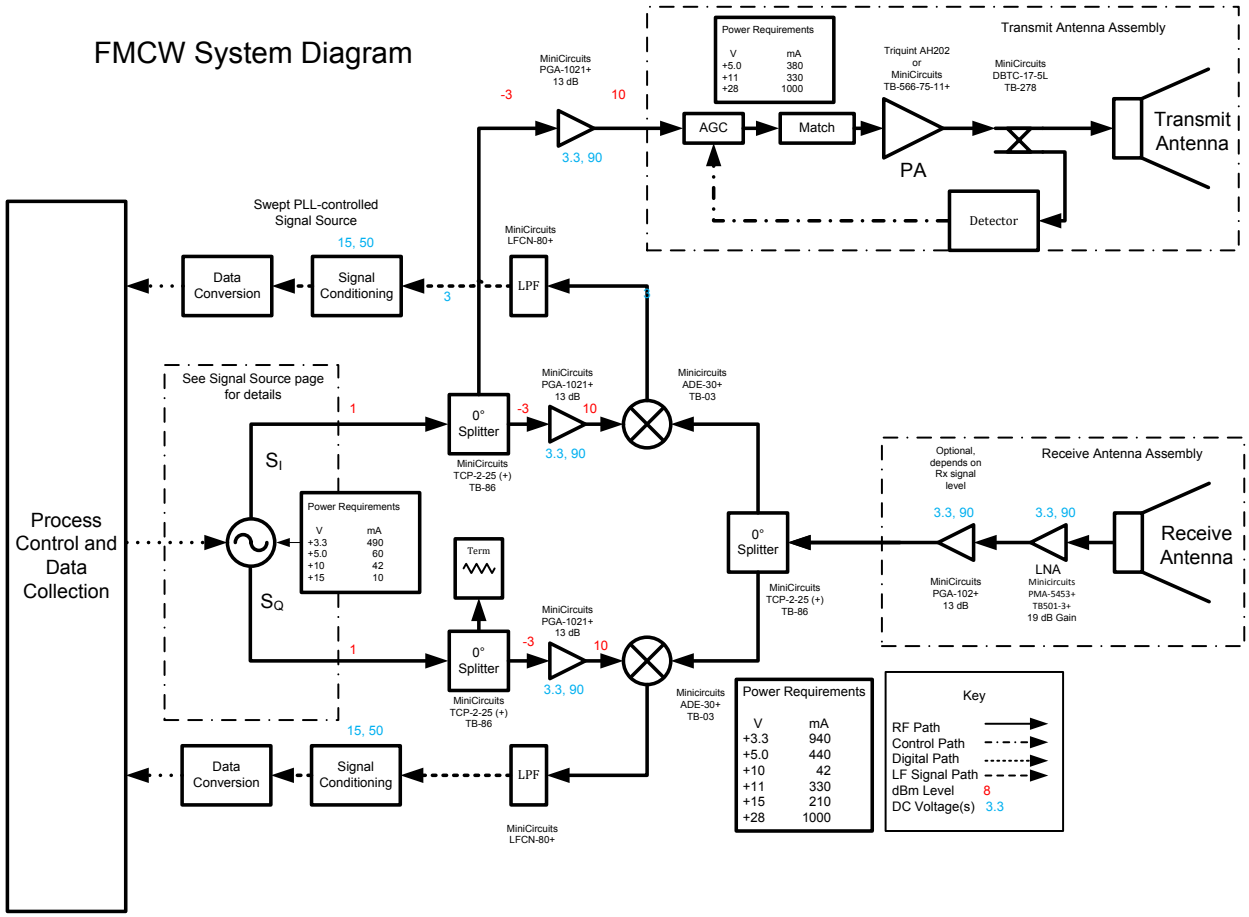

Figure 1 System Block Diagram

Frequency Source

A key component of this system is the frequency source and its control. The operating frequency spans two octaves over a frequency range where the use of a single oscillator is not a good option. YIG oscillators do not function well at 500 MHz, and the frequency range of varactor-tuned oscillators is generally limited to around 1 octave due to the limitations of a 4:1 capacitance range of a varactor capacitor. The use of frequency dividers to increase the range does not support the capabilities of a continuous sweep over the desired range.

For these reasons, a heterodyne system was chosen as the preferred design, as shown in Figure 2. To reduce spurious signals based on mixing products and to take advantage of the tuning non-linearities to support the wideband PLL (as discussed later), the heterodyne design was chosen to use a high-side LO from a narrow-band oscillator and to derive the frequency by downconverting the wide-band VCO. The choice of frequencies is a tradeoff as higher frequency oscillators will generally result in reduced spurious mixing product but lower frequency oscillators will generally provide a lower level of phase noise. Phase noise in an FMCW system can cause SNR degradation in the resulting IF signal [1]. The predominant

[1] Beasley, Patrick, "The Influence of Transmitter Phase Noise on FMCW Radar Performance," Proceedings of the 3rd European Radar Conference, September 2006, pp. 331-334.

cause of the degradation is the coupling of significant reflections that may dominate the desired reflection being analyzed. One significant potential source of such unwanted signals in a 2-antenna system is crosstalk or coupling that may occur between the antennas.

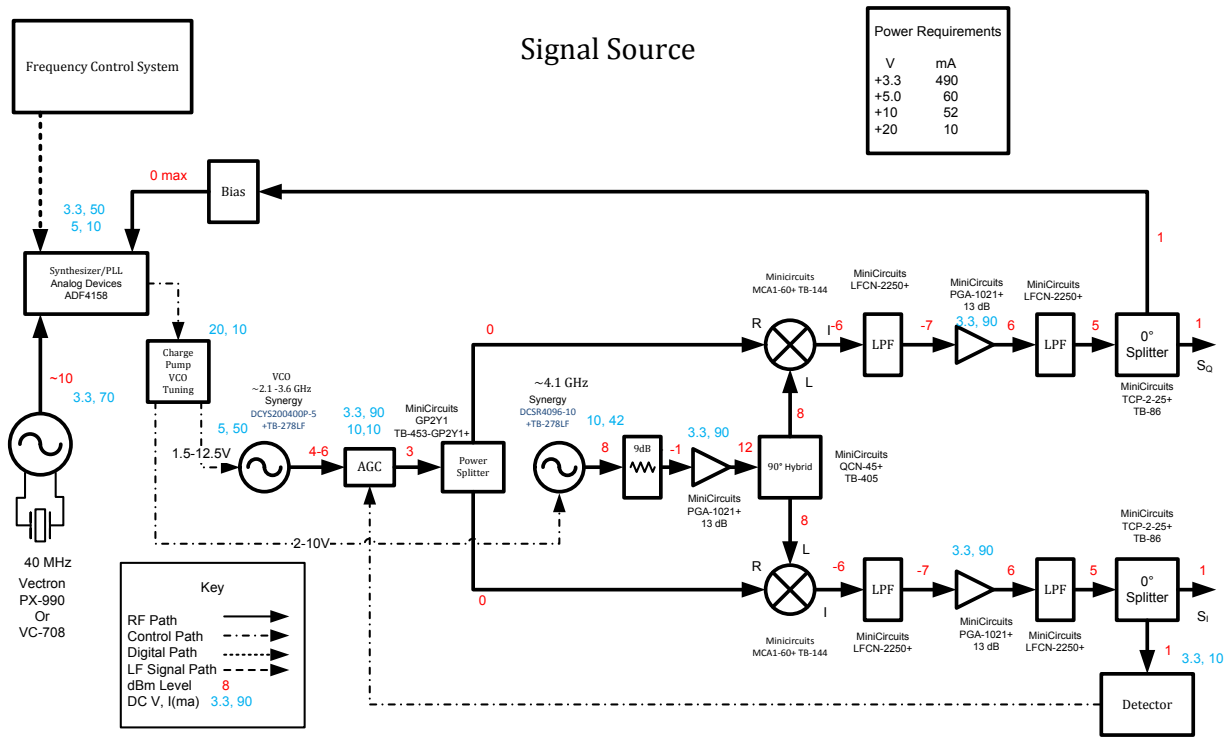

Figure 2 RF Signal Source

The initial choice for this system is to operate the local oscillator frequency at about 4.1 GHz and to operate the wideband oscillator over a range of 2.1 – 3.6 GHz, yielding a resulting difference frequency of 500 MHz – 2 GHz. The design can be altered by changing a few components to support higher frequencies for both oscillators to yield the same range of output frequencies.

For this design, the frequency range is achieved using two relatively low-phase-noise standard VCOs from Synergy Microwave. These were chosen because of their inherently superior unlocked phase noise, allowing the locked oscillators to achieve better phase noise results, particularly at higher offset frequencies. VCO1 is a model DCYS200400-5, which can be tuned from 2.0 – 4.0 GHz and VCO2 is a model DCSR4096-10 which can be tuned to 4.096 GHz ± 10 MHz. These two sources are mixed to produce an output frequency of $f_{VCO2} - f_{VCO1}$. One PLL approach would have been to provide an independent PLL for each VCO prior to mixing the signals. This approach adds the complexity of two PLL systems, creates greater phase noise due to the summing of the phase detector noises for the two PLLs, requires both PLLs to operate at higher frequencies where their phase noise performance is typically worse due to higher divide ratios, and adds makes the typically non-linear tuning curve for the VCO1 more problematic in the loop design.

The PLL chosen is an Analog Devices ADF4158, which is a recent (introduced in 2010) device specifically targeted for FMCW systems. This device contains a variety of features that are specifically intended for FMCW products. These features include the capability to program both sawtooth and triangular ramps, optional capability to program dual slope ramps, and the ability to include FSK features into the ramp. The device is based on a fractional-N divider, and for this design the plan is to operate the

phase-frequency detector (PFD) at a 20 MHz rate. The 20 MHz reference signal is derived from a low phase noise Crystek 80 MHz crystal oscillator.

The use of a PLL to control a swept FMCW signal source is involves some unusual concepts. The classic PLL system is designed to drive the VCO to a stable frequency and maintain it at that frequency with minimal spectral sidebands. That is clearly not the desired result for an FMCW source where the objective is a linear, continuous frequency sweep. The standard approach of reaching stable frequencies is generally not desired. However, if properly designed, the PLL system should be able to improve both the sweep linearity and the phase noise of the source.

The loop is designed to update the desired frequency at a 20 MHz rate while sweeping, and the loop bandwidth of the PLL is designed to be 200 kHz. The loop bandwidth is chosen to minimize phase noise over the range of interest, and increasing it above that frequency would cause higher phase nose at 200 kHz offset and above. Furthermore, the fact that the loop bandwidth is two orders of magnitude less than the update rate will lead to very nearly linear frequency sweeps as the loop will have virtually no step response to the frequency steps issued at the 20 MHz update rate.

The PLL is implemented with the objective of providing excellent frequency ramp linearity and low phase noise over the critical range of 100Hz to 100 kHz. The low end of the critical phase noise is determined by the slowest anticipated frequency ramp time of approximately 10 ms and the top end is determined by the highest anticipated frequency component. Analysis (see (9) in Appendix A) and simulations show that for a frequency ramp of 1.5GHz/2ms (probably the fastest reasonable), the resulting IF frequency will be 5 kHz/meter (one-way distance in air).

The approximate phase noise of the unlocked VCO combination (per the data sheet) is shown in Figure 3 and the simulated locked phase noise, with the contributions by the various loop components, is shown in Figure 4

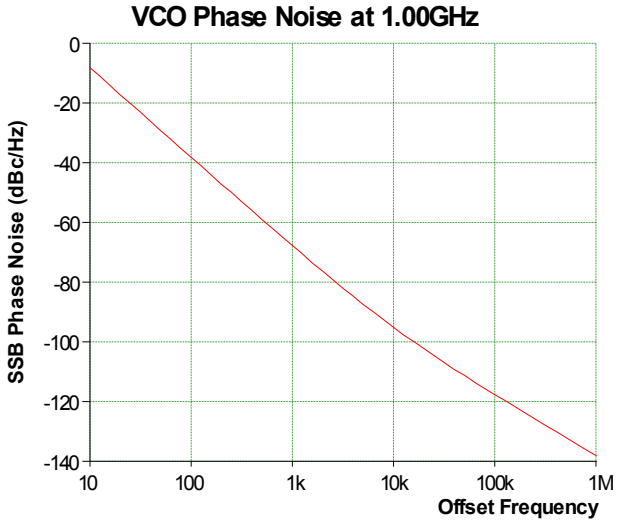

Figure 3 Phase noise of unlocked VCO system

As can be seen in Figure 4, the PLL provides a significant reduction in phase noise at offset frequencies below approximately 20 kHz.

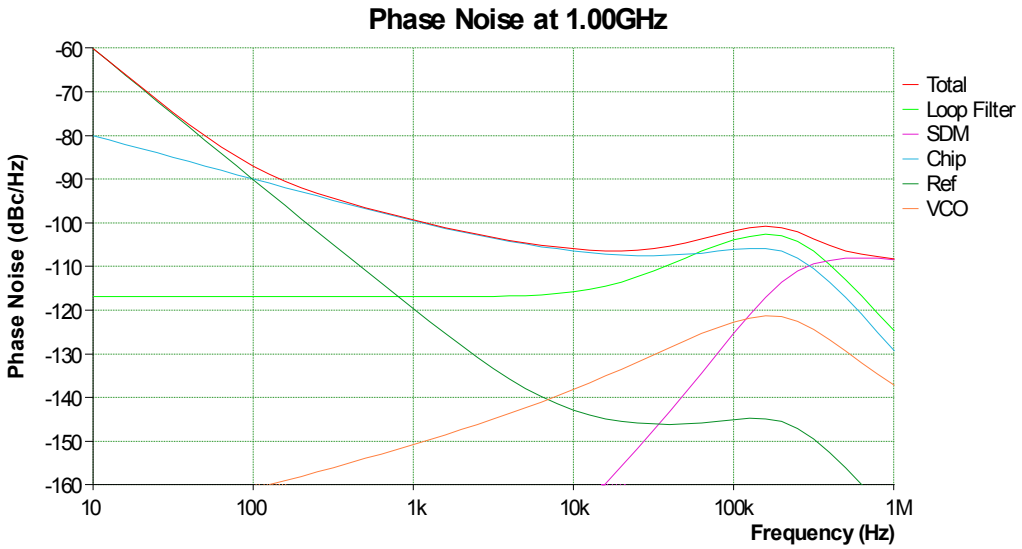

Figure 4 Simulated phase noise of locked VCO

A challenge from the use of a PLL covering two octaves is the need to assure proper gain compensation due to the fact that the frequency division ratio N will vary over a 4:1 range. This division ratio appears as an inverse factor in the PLL loop gain, and must be considered as a loop stability factor. Fortunately, downconversion of the wideband oscillator helps to solve this problem because the tuning nonlinearity helps to compensate for this gain variation. This nonlinearity is shown in Figure 5 where the VCO tuning nonlinearity shown in the blue (Fosc) plot translates through the downconversion process (Fout = 4.1 GHz – Fosc) into the red curve.

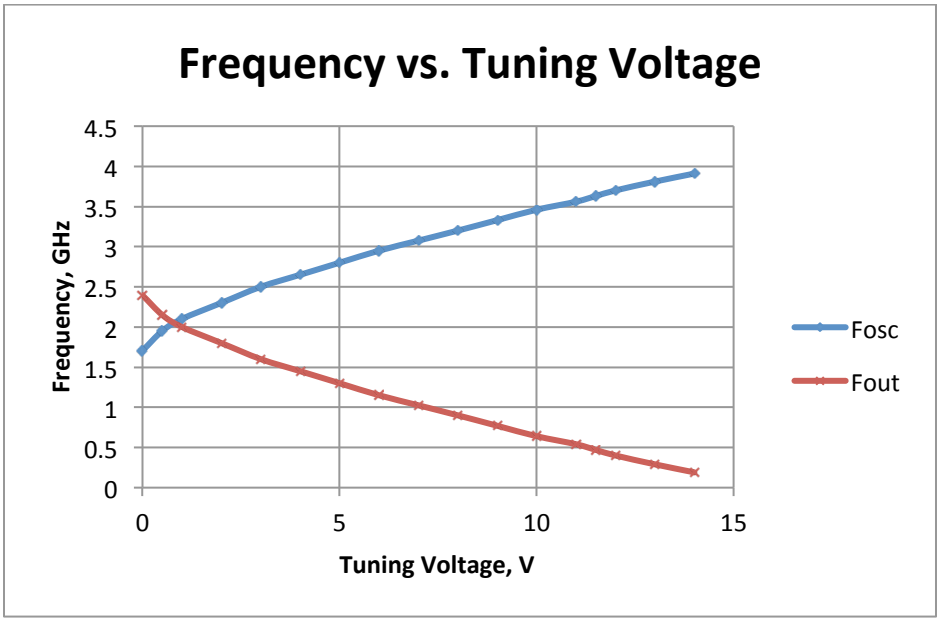

Figure 5 VCO Frequency vs. Tuning Voltage

From the perspective of the PLL loop design, it is important to consider how this impacts the variation of the loop gain. To do this, we begin by determining the slope of the tuning curve, or the sensitivity in MHz/Volt as shown in Figure 6. Bear in mind that this is the reverse of the actual VCO tuning curve because the frequency is mirrored due to the mixing with the 4.1 GHz oscillator.

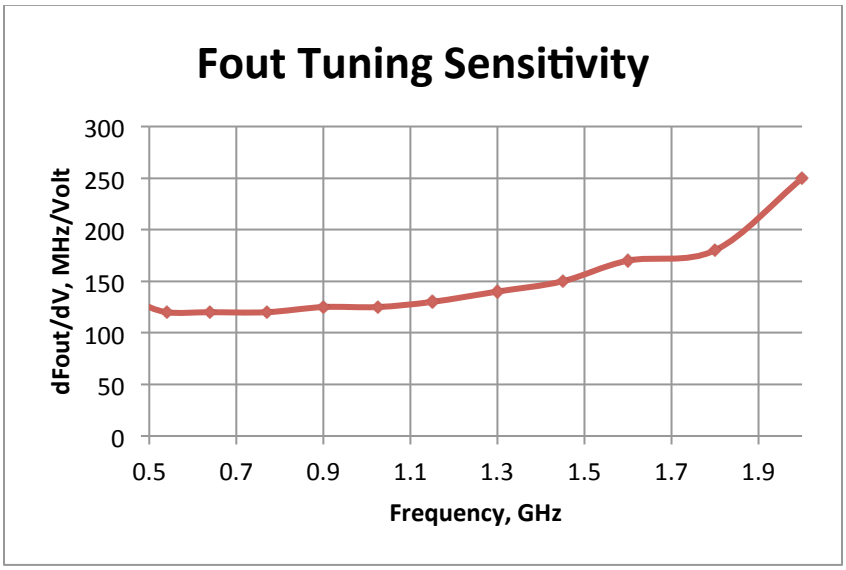

Figure 6 Tuning sensitivity of the downconverted VCO

This frequency is divided by a factor N (which in the case of the fractional N synthesizer, is not necessarily an integer). Because the frequency presented to the PFD is this divided frequency, the division ratio must be considered in the loop gain. In the case of this design with the nominal PFD frequency of 80 MHz, the value of N is Fout(Mhz)/80. This result is shown in Figure 7.

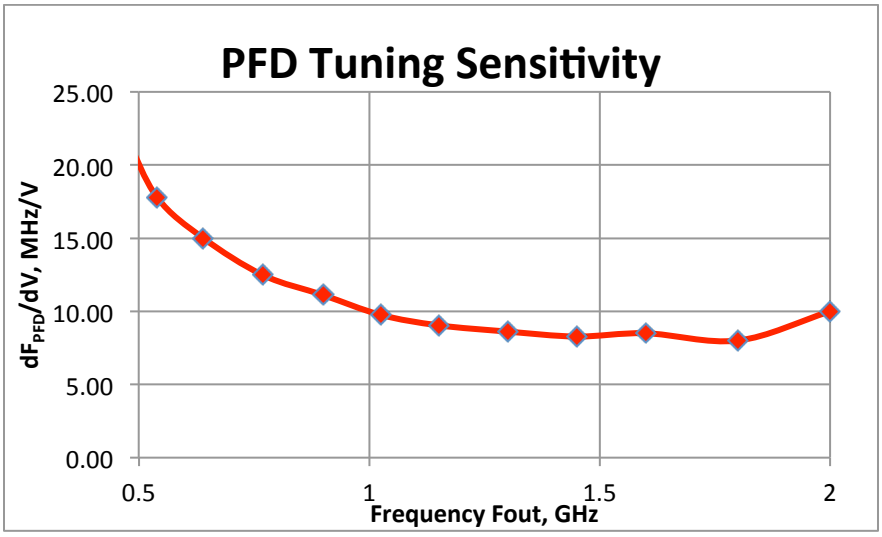

Figure 7 PFD Tuning Sensitivity

As can be seen, this will result in a loop gain variation of greater than 2:1 over the range of operation. The loop can be designed to be stable with this variation, but a more consistent gain crossover frequency and therefore better performance can be achieved by doing a minor correction of the tuning curve using simple diode shaping. One example of how this might be done is shown in Figure 8 where the use of two shaping diodes can easily reduce the gain variation.

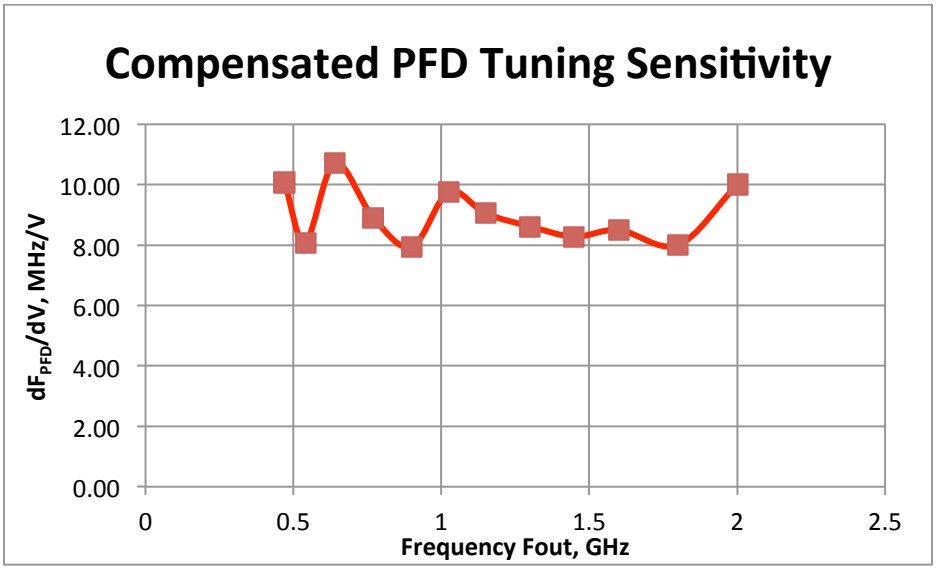

Figure 8 Compensated PFD Tuning Sensitivity

Appendix A – Design details

A first article implementation of the entire solution has been created through the schematic diagrams below, followed by the layout of the PCBs, followed by the fabrication and assembly of the boards.

Early testing has suggested that the original design of the power regulator, which incorporated switching power supplies, will be difficult to shield effectively to prevent the injection of noise in the system. As a result, this module has been redesigned and will be constructed and tested shortly.

The RF source section in Figure 9 includes the two VCOs, gain stages, splitters and the quadrature mixers, and linear regulators to provide low-noise power to the devices from the common supply module.

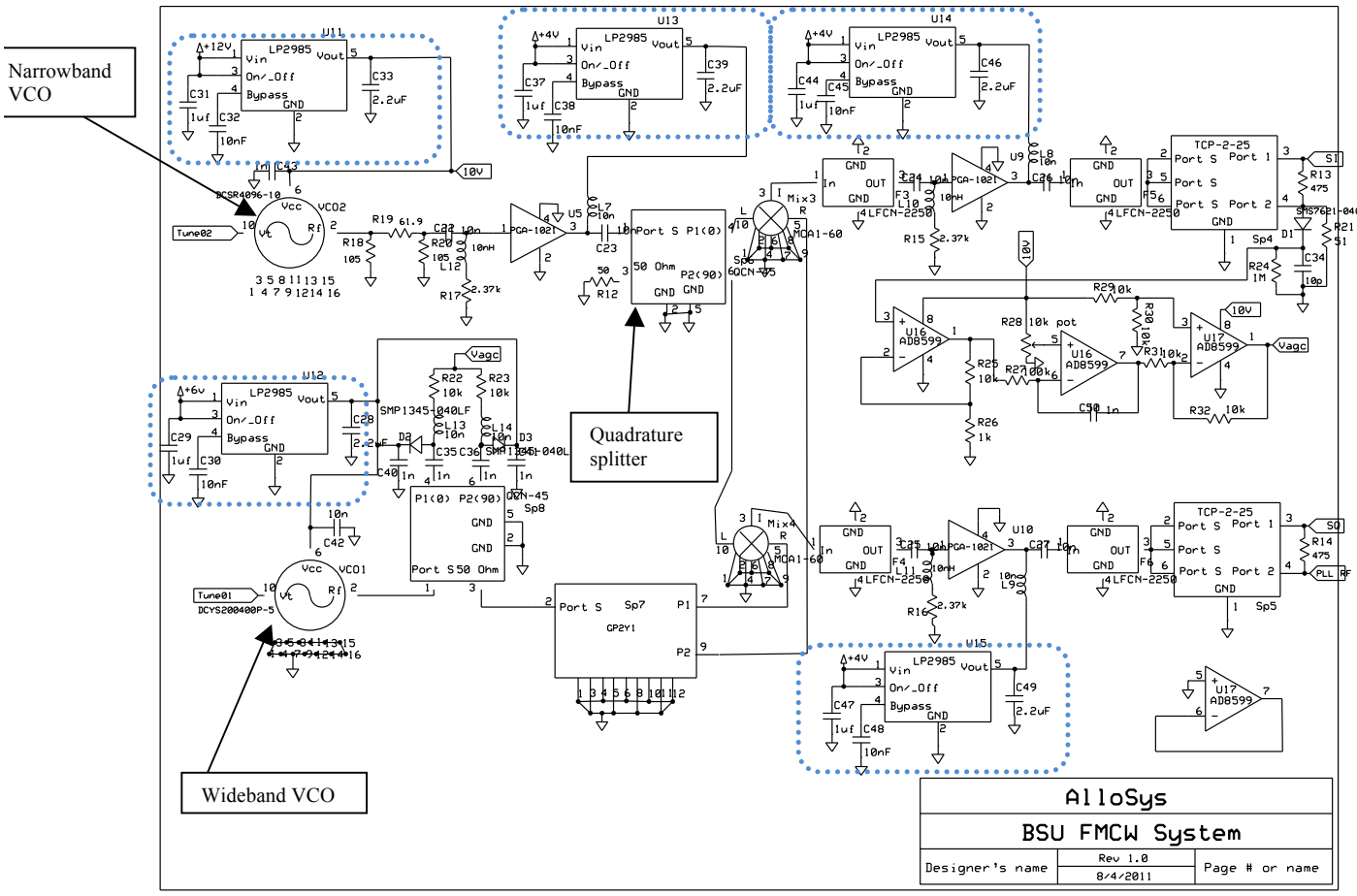

Figure 9 Schematic diagram for the RF Source Section

The circuits in Figure 10 show the receive section including the splitter and the quadrature mixers, and the low-noise IF gain channels to condition the IF signal for the A/D converter. In addition, it shows the splitters for the Tx signal to power the Tx antenna and to serve as the LO for the Rx mixers.

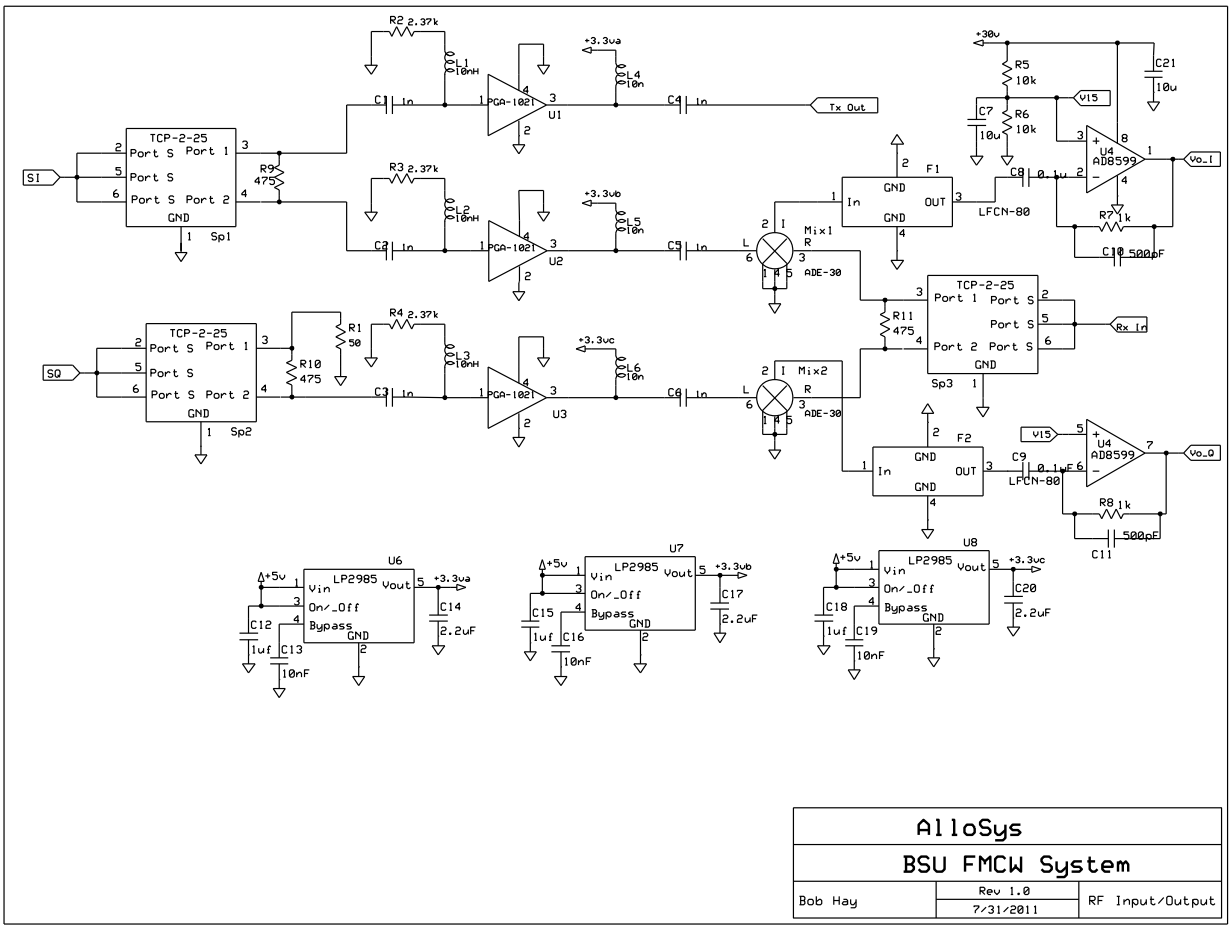

Figure 10 Schematic diagram for the RF I/O and Rx section

The synthesizer board circuit is shown in Figure 11. The major components of this circuit are the systhesizer chip, the reference oscillator, the supporting low-noise power regulators, and the I/O buffer to protect the synthesizer from external transients. Note that the I/O buffer, which is a standard CMOS hex inverter, operates at 3.3 volts so that it can interface with the synthesizer. However, due to its input protection diodes, it can be driven with a 5 volt digital signal as long as there is at least 1k of resistance between the digital output signal and the input to the hex inverter.

This circuit has an RF input from the PLL output from the circuit in Figure 9 and creates the charge pump (CP) source for the circuit in Figure 11

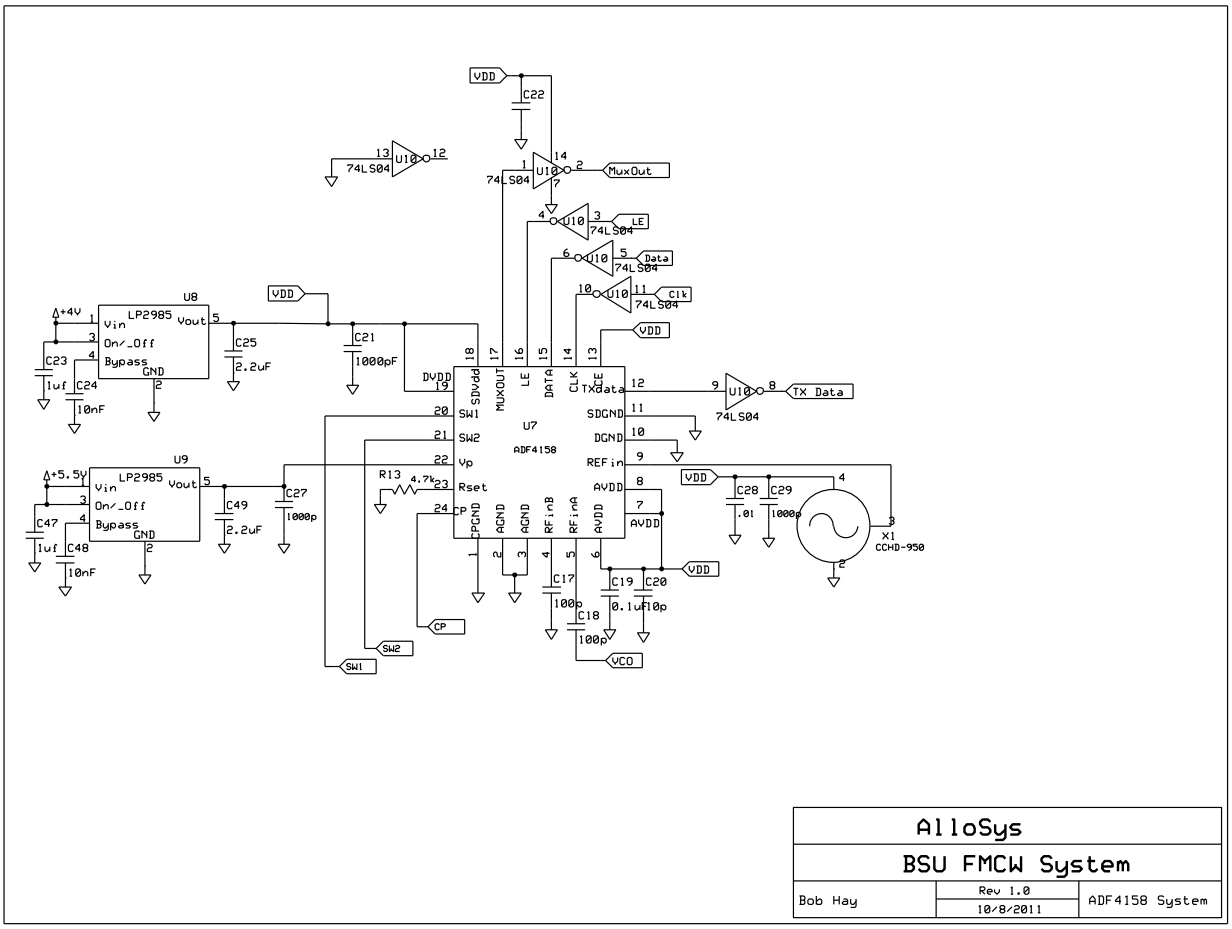

Figure 11 ADF 4158 Synthesizer Circuit

In Figure 12 is shown the tune compensation circuit. This design incorporates a second-order PLL where the circuit inserts a low-frequency zero in the loop to maintain a relatively wide bandwidth and then a higher-frequency pole to achieve the desired gain crossover. This design will likely be modified as necessary to achieve the optimum performance. This circuit generates the tune voltages used by both VCOs.

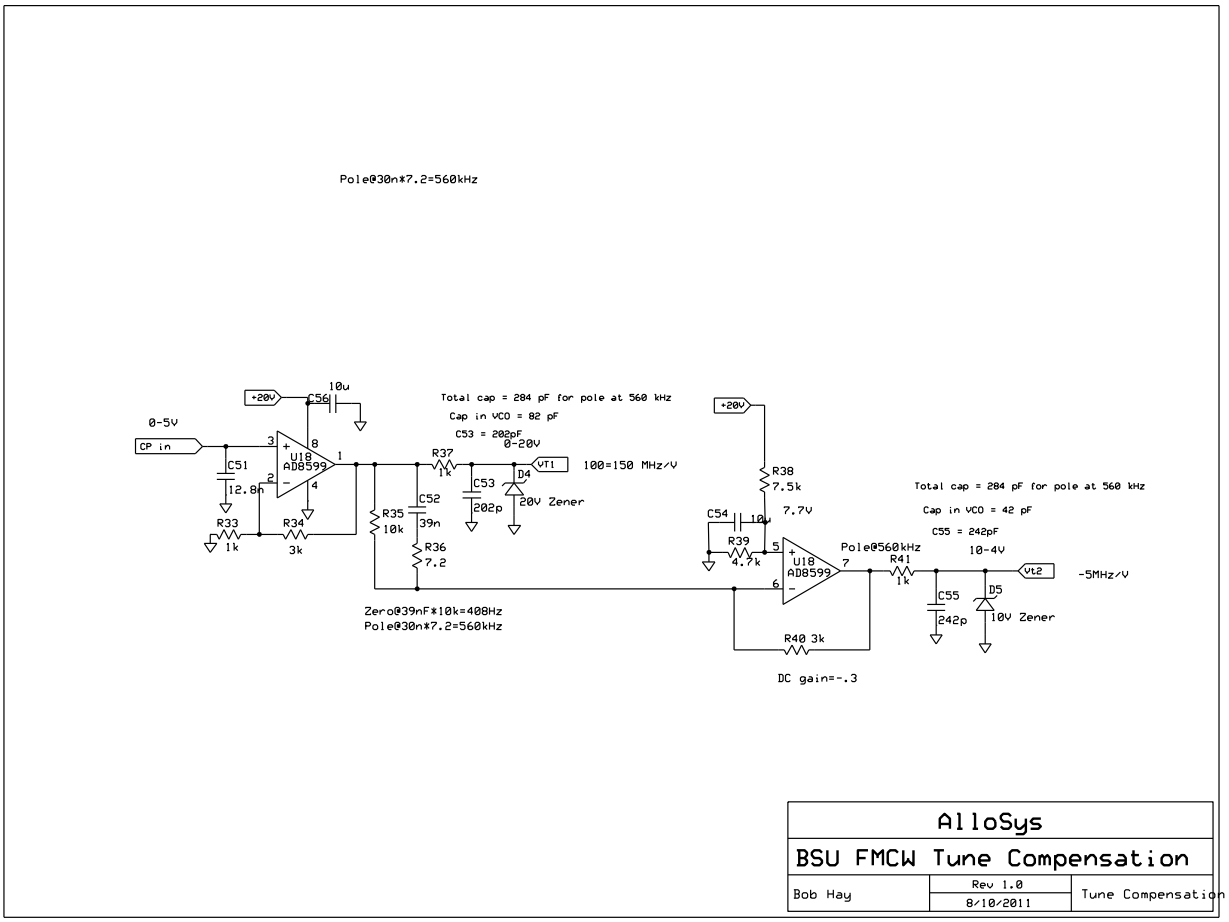

Figure 12 Tune compensation circuits

The LNA circuit is shown in Figure 13. This incorporates a LNA amplifier chip which is specified to have a noise figure of less than 2 dB over the operating frequency range.

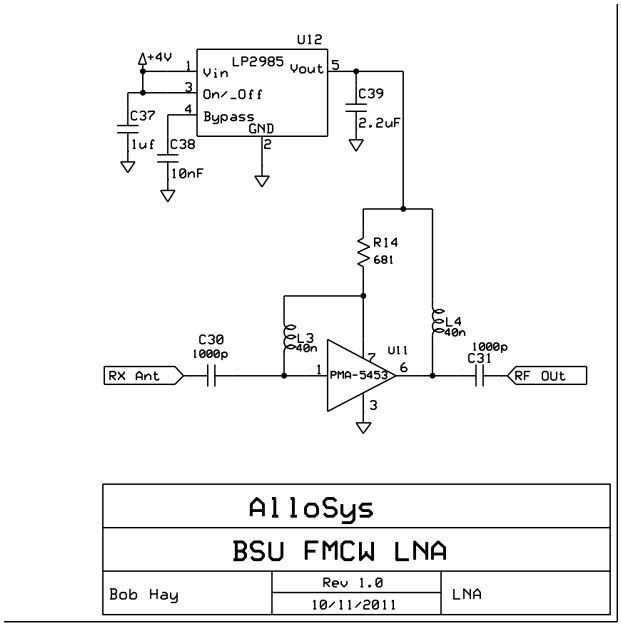

Figure 13 LNA Circuit

The custom PCB layout for the RF portion of the system is shown in Figure 14. This includes the circuits shown in the schematic diagrams from Figure 9, Figure 10, and Figure 12.

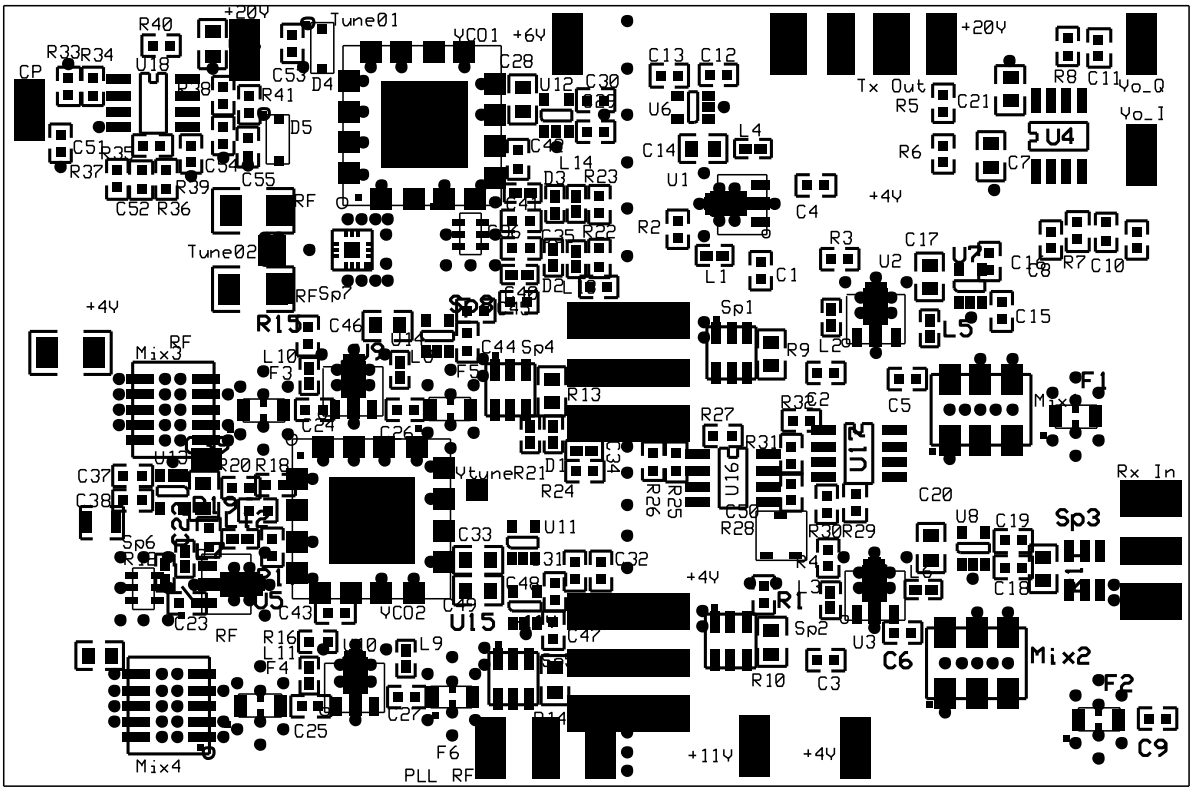

Figure 14 RF PCB Layout

The loaded board is shown in Figure 15. The orientation of this photograph is rotated 180° from the layout shown in Figure 14.

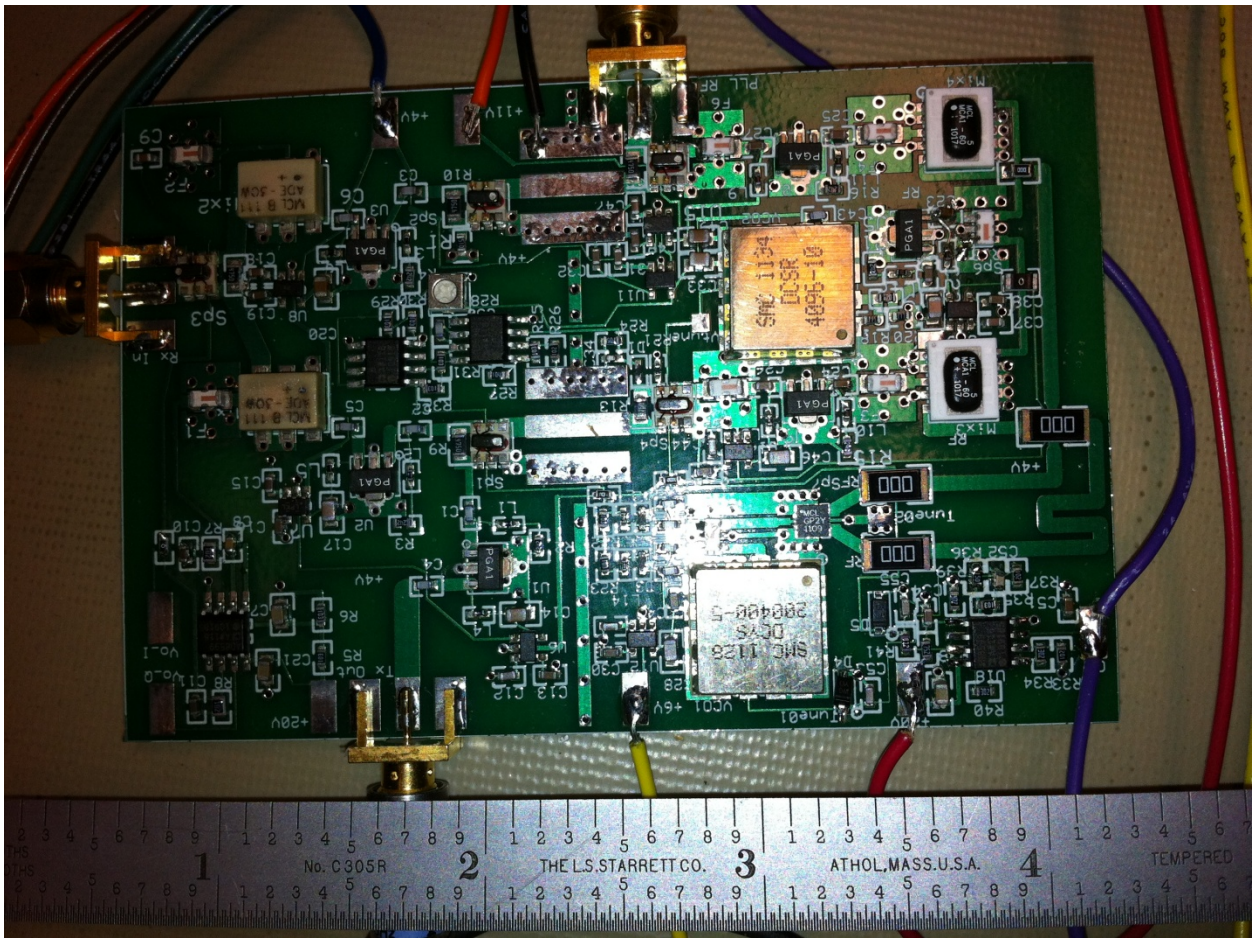

Figure 15 The RF Board

A PCB that contained a first-pass layout for the power regulator, the LNA, the synthesizer board, and the power regulators was laid out and fabricated as shown in Figure 16. The assembled synthesizer is shown in Figure 17 and the assembled regulator is shown in Figure 18.

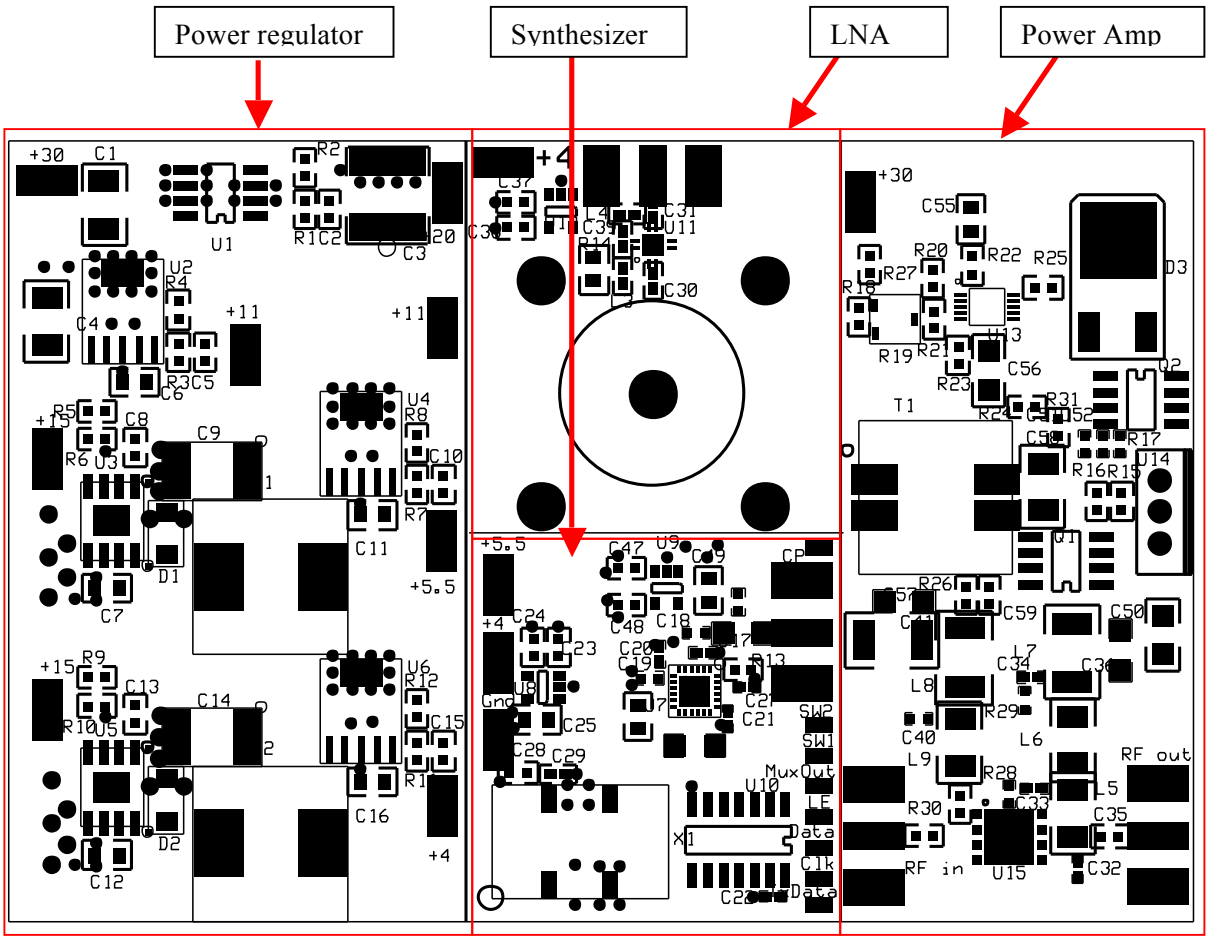

Figure 16 PCB Layout for Power Regulator, LNA, Synthesizer, and PA

The Synthesizer board uses the RF input and the Crystal reference oscillator along with the programmed division ratio to create the charge pump output that controls the VCOs on the RF board.

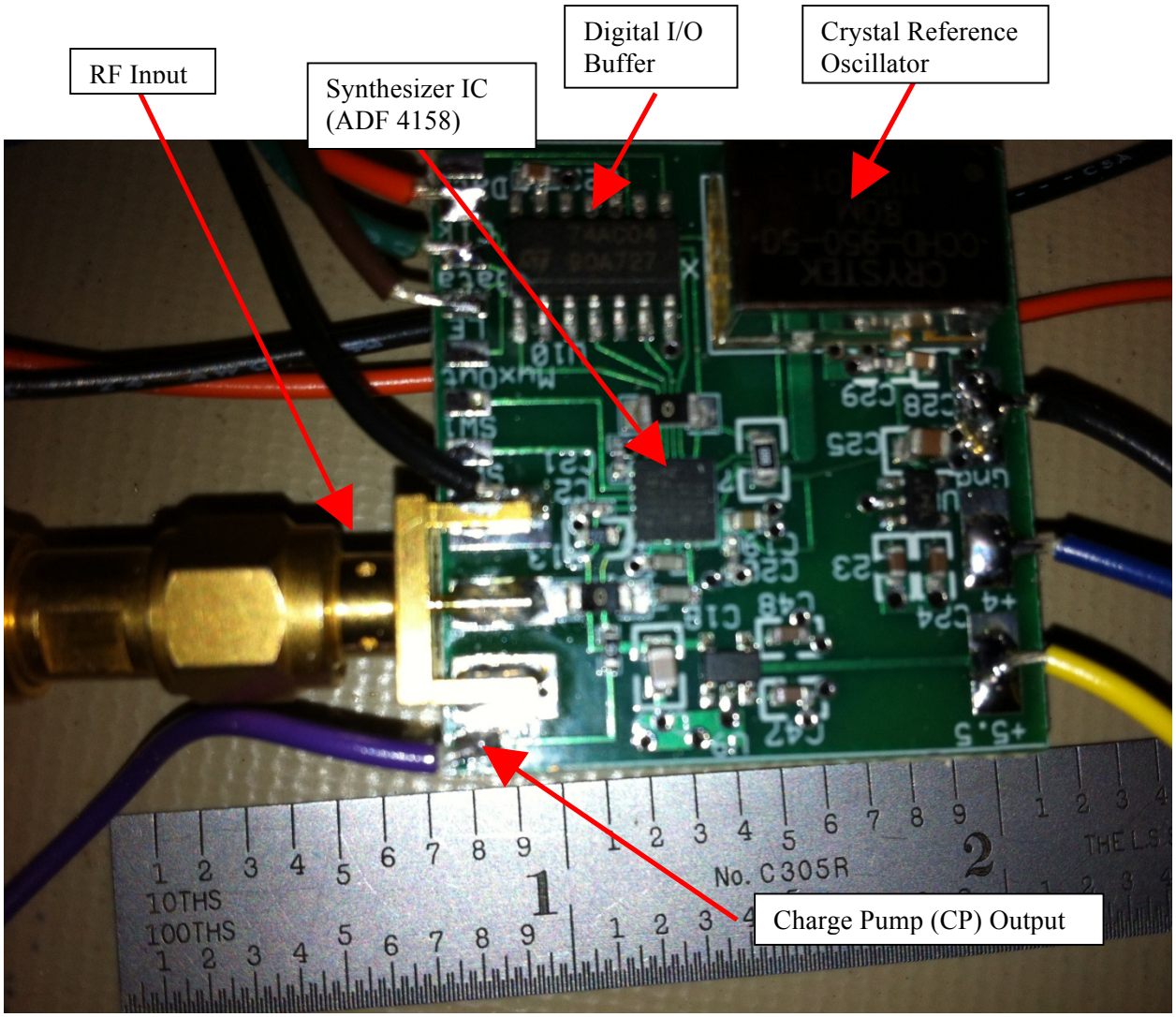

Figure 17 Synthesizer Board

The power regulation board is needed to provide voltage outputs of +20V, +11V, +5.5V, and +4V. These voltages are then typically regulated to +20, +10, +5, and +3.3 V for the loads. The initial voltage regulation board is shown in Figure 18. This board uses switching regulators to supply the +5.5 and +4 V sources. The design worked well except for the classic problem that it is difficult to deal with the high frequency noise associated with switching regulators in RF systems. The use of local linear regulators for the individual devices would generally solve this problem, but the electromagnetic radiation from the inductors in the regulator A new layout which includes only linear regulators has been submitted and will be constructed shortly.

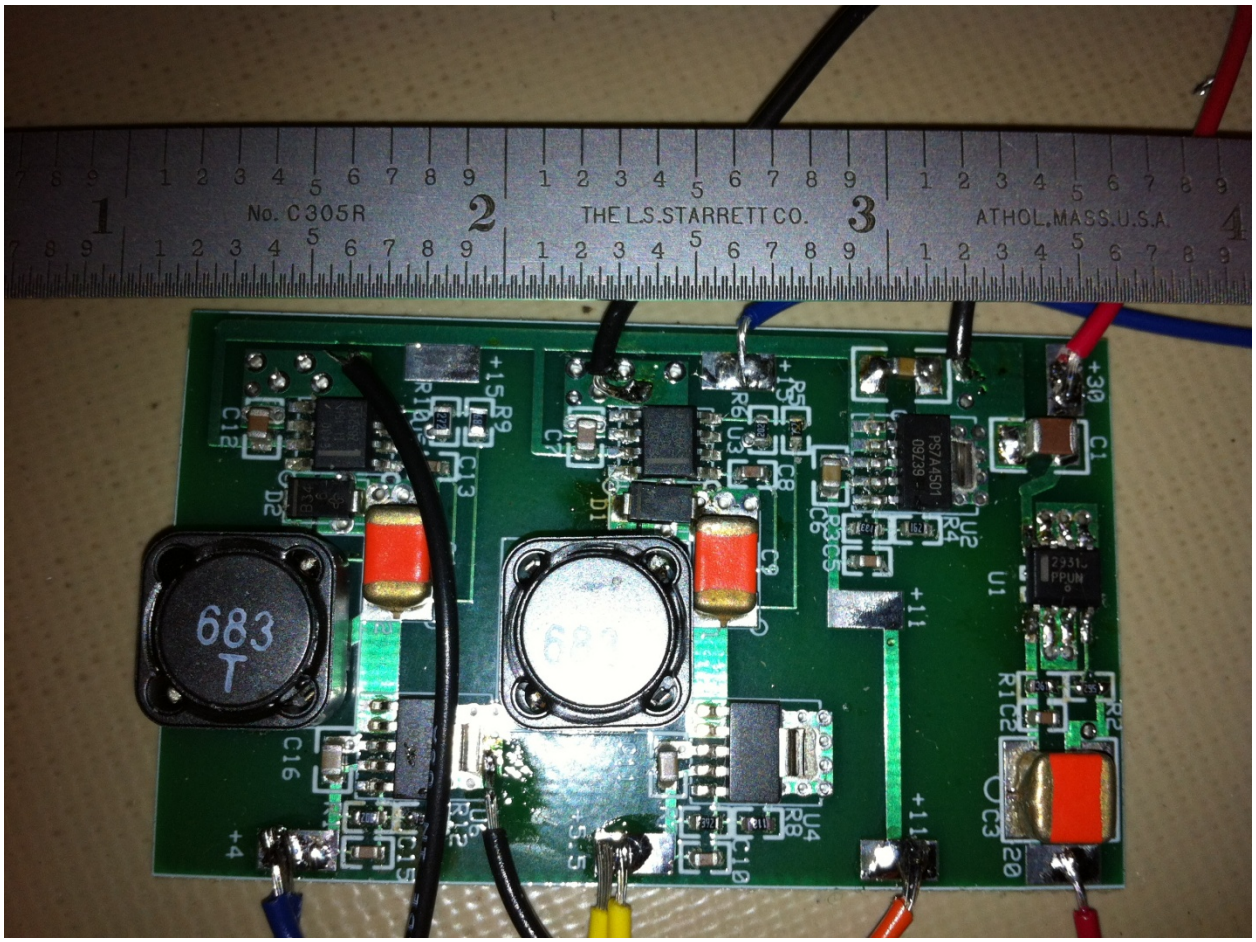

Figure 18 Initial Voltage Regulation Board

The revised schematic incorporating the linear regulator is shown in Figure 19 and the layout is shown in Figure 20

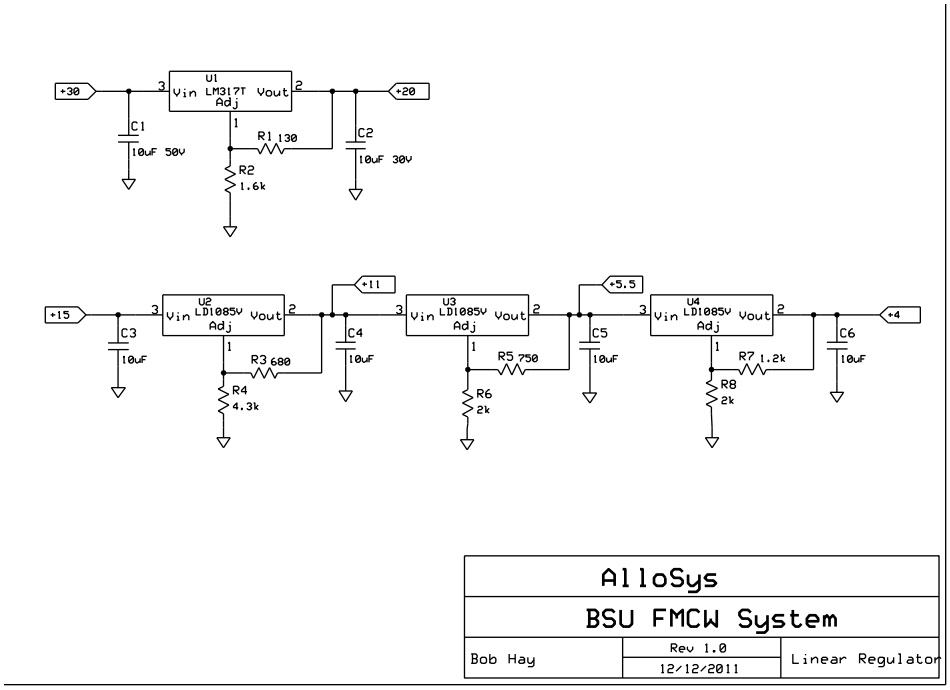

Figure 19 Linear Regulator Schematic

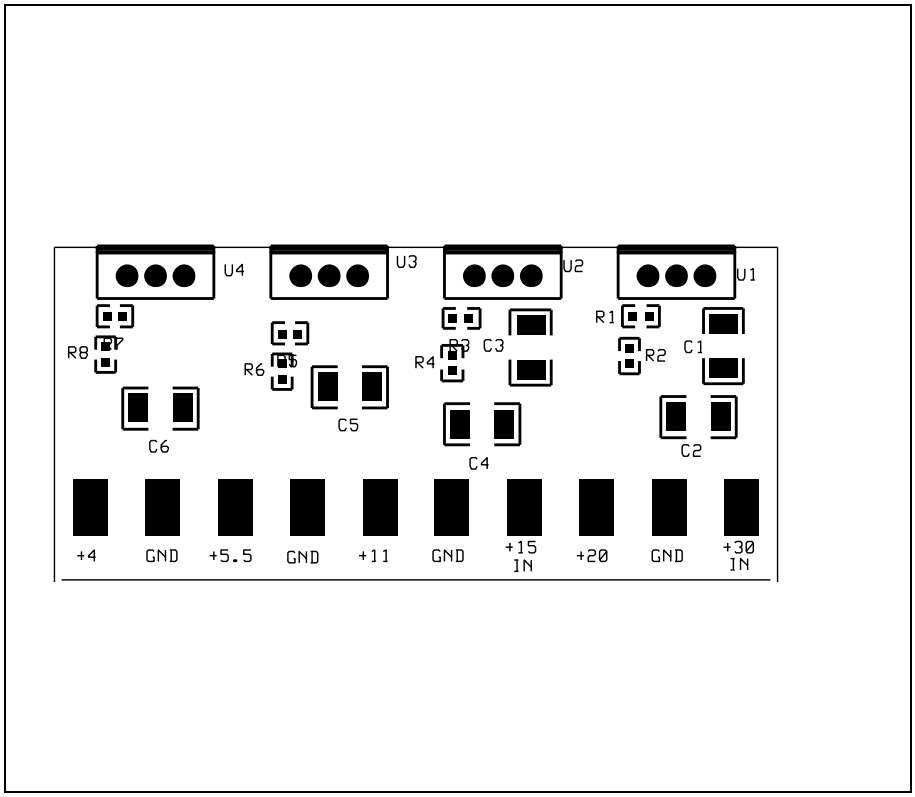

Figure 20 Linear Regulator Layout

Appendix B.

This analysis assumes a linear FMCW system which sweeps linearly from an initial frequency ω_C to a higher frequency which is not initially determined. The initial analysis does not consider the benefits of a triangular sweep that offers the ability to correct for Doppler shift due to distance motion between the Radar system and the target.

For a fundamental linear FMCW system where the radian frequency sweep rate is

$$\alpha = \frac{d\omega}{dt} \text{ radians/sec}^2 \tag{1}$$

The transmitted signal s_T can then be represented as

$$s_T = \cos(\omega_C t + \varphi_M) \tag{2}$$

where ω_C is the carrier frequency and φ_M is the phase modulation necessary to develop the linear frequency sweep. Clearly, since phase is the integral of frequency, it is easily shown that

$$\varphi_M = .5\alpha t^2 \tag{3}$$

so that (assuming unity peak amplitude)

$$s_T = \cos(\omega_C t + .5\alpha t^2) \tag{4}$$

Assume that the return signal is delayed by time τ and is furthermore shifted in the reflection by angle θ_{REFL}. Given a propagation velocity c and a distance d to the target, this roundtrip delay is

$$\tau = \frac{2d}{c} \tag{5}$$

The resulting received signal (ignoring loss of signal) would then be

$$s_R = \cos(\omega_C(t-\tau) + .5\alpha(t-\tau)^2 + \theta_{REFL}) \tag{6}$$

where θ_{REFL} is the phase shift added by the reflection interface. Multiplying the transmitted and received signals (as in a mixing process) and selecting the lower sideband, the resulting IF signal would be determined by the subtraction of the two cosine arguments

$$s_{IF} = \cos(\omega_C\tau + \alpha\tau t - .5\alpha\tau^2 + \theta_{REFL}) \tag{7}$$

This can be rearranged as

$$s_{IF} = \cos(\alpha\tau t + \omega_C\tau - .5\alpha\tau^2 + \theta_{REFL}) \tag{8}$$

from which it can be seen that the radian frequency of the IF signal is

$$\omega_{IF} = \alpha\tau \tag{9}$$

and the phase of the IF signal is

$$\emptyset_{IF} = \omega_C\tau - .5\alpha\tau^2 + \theta_{REFL} \tag{10}$$

For a single reflection object that causes a radian frequency ω_{IF} , it can be easily determined that the distance to the reflection object is

$$d = \frac{v\tau}{2} = \frac{v\omega_{IF}}{2\alpha} \tag{11}$$

where the propagation velocity

$$v = \frac{c}{\sqrt{\varepsilon_r \mu_r}} = \frac{c}{n} \tag{12}$$

where c is the electromagnetic velocity in a vacuum, and ε_r and μ_r are the relative permittivity and permeability respectively and n is the index of refraction of the medium. Note that all three of these values may be complex, with the imaginary component being related to signal absorption in the material. For most radio wave applications, it is reasonable to assume that $\mu_r \approx 1$. It can also be seen by combining (9) and (10) that the reflection angle is

$$\theta_{REFL} = \emptyset_{IF} - \frac{\omega_C}{\alpha}\omega_{IF} + \frac{.5}{\alpha}(\omega_{IF}{}^2) \tag{13}$$

Resolution

The discrete Fourier Transform frequency resolution is

$$\Delta f_{IF} = \frac{1}{T_s} \tag{14}$$

where T_s is the total sample time for a frequency sweep.

Suppose there are two reflections that occur at distances d_1 and d_2 such that $\Delta d = d_2 - d_1$.

From (11),

$$\Delta d = \frac{v}{2\alpha}\Delta\omega_{IF} \tag{15}$$

and since

$$\Delta\omega_{IF} = 2\pi\Delta f_{IF} \tag{16}$$

the resulting resolution is

$$\Delta d = \frac{\pi c}{\alpha}\frac{1}{T_s} \tag{17}$$

Noting from (1) that the extent of the sweep, which is approximately bandwidth β in Hz is

$$\beta = \frac{\alpha\, T_s}{2\pi} \tag{18}$$

it is then apparent by substituting (18) into (17) that

$$\Delta d = \frac{v}{2\beta} \tag{19}$$

which is exactly the minimum expected resolution for a Radar system. Note that since the coherence length of a modulated signal is generally defined as

$$L = \frac{v}{\beta} \tag{20}$$

then

$$\Delta d = \frac{L}{2} \tag{21}$$

Quadrature

For a quadrature demodulator, the LOq signal would be

$$s_{LOq} = \sin(\omega_C(t - dt) + .5\alpha(t - dt)^2) \tag{22}$$

Given that

$$\sin x \cos y = .5[\sin(\mathrm{x} + \mathrm{y}) + \sin(\mathrm{x} - \mathrm{y})] \tag{23}$$

the lower sideband of the IF signal, ignoring the amplitude factor, would be

$$s_{IFq} = \sin(\alpha\tau t + \omega_C\tau - .5\alpha\tau^2 + \theta_{REFL}) \tag{24}$$

which, as expected, is the s_{IF} signal of (8) rotated by 90° .